

EPIC 219217635: a doubly eclipsing quadruple system containing an evolved binary

T. Borkovits,^{1,2★} S. Albrecht,³ S. Rappaport,⁴ L. Nelson,⁵ A. Vanderburg,^{6,7†} B. L. Gary,⁸ T. G. Tan,⁹ A. B. Justesen,³ M. H. Kristiansen,^{10,11} T. L. Jacobs,¹² D. LaCourse,¹³ H. Ngo,^{14,15} N. Wallack,¹⁵ G. Ruane,^{16‡} D. Mawet,¹⁷ S. B. Howell¹⁸ and R. Tronsgaard^{19,20}

Affiliations are listed at the end of the paper

Accepted 2018 May 23. Received 2018 May 20; in original form 2018 May 6

ABSTRACT

We have discovered a doubly eclipsing, bound, quadruple star system in the field of K2 Campaign 7. EPIC 219217635 is a stellar image with $K_p = 12.7$ that contains an eclipsing binary (EB) with $P_A = 3.59470$ d and a second EB with $P_B = 0.61825$ d. We have obtained follow-up radial velocity (RV) spectroscopy observations, adaptive optics imaging, and ground-based photometric observations. From our analysis of all the observations, we derive good estimates for a number of the system parameters. We conclude that (1) both binaries are bound in a quadruple star system; (2) a linear trend to the RV curve of binary A is found over a 2-yr interval, corresponding to an acceleration, $\dot{\gamma} = 0.0024 \pm 0.0007$ cm s⁻²; (3) small irregular variations are seen in the eclipse timing variations (ETVs) detected over the same interval; (4) the orbital separation of the quadruple system is probably in the range of 8–25 au; and (5) the orbital planes of the two binaries must be inclined with respect to each other by at least 25°. In addition, we find that binary B is evolved, and the cooler and currently less massive star has transferred much of its envelope to the currently more massive star. We have also demonstrated that the system is sufficiently bright that the eclipses can be followed using small ground-based telescopes, and that this system may be profitably studied over the next decade when the outer orbit of the quadruple is expected to manifest itself in the ETV and/or RV curves.

Key words: binaries: close – binaries: eclipsing – binaries: general.

1 INTRODUCTION

Quadruple or higher order multiple systems constitute a relatively small but very important fraction of gravitationally bound, few-body stellar systems. For example, according to the distance-limited ($D \leq 75$ pc) sample of De Rosa et al. (2014) the lower limit on the frequency of quadruple or higher order multiple systems¹ having an A-type star as the more massive component is about 2.5 per cent. Investigating a similar distance-limited ($D \leq 67$ pc) collection of FG dwarf multiples, Tokovinin (2014) found the same occurrence frequency to be 4 per cent. The majority of the known quadruple stars form a 2 + 2 hierarchy, i.e. two smaller separation (and, there-

fore, shorter period) binaries that orbit around their common centre of mass on a much wider, longer period orbit. For example, in the previously mentioned sample of FG multiples, 37 of the 55 quadruple stars have the 2 + 2, double binary configuration. Furthermore, quadruple subsystems of higher order multiple star systems also often come in the form of a 2 + 2 hierarchy.

Double binary systems are important tracers of stellar formation scenarios. Their mass and period ratios, as well as their flatness (i.e. the inclination of the outer orbit relative to the two inner ones), may carry important information on their formation processes, as well as their further evolution (see e.g. Tokovinin 2008, 2018, and references therein).

Another interesting aspect of double binaries is their dynamics, i.e. long-term orbital evolution. Recent analytical (Fang, Thompson & Hirata 2018) and numerical (Pejcha et al. 2013) studies have pointed out that 2 + 2 quadruples with an inclined outer orbit may be subject to Kozai–Lidov cycles (Kozai 1962; Lidov 1962) that reach higher eccentricities than triple stars. This can result, amongst

* E-mail: borko@electra.bajaobs.hu

† NASA Sagan Fellow.

‡ NSF Astronomy and Astrophysics Postdoctoral Fellow.

¹In these surveys single A-, F-, or G-type stars are to be counted as ‘systems’.

other interesting phenomena, in dramatic inner binary eccentricity oscillations that temporarily might produce extremely high eccentricities (such as e.g. $e_{\text{in}} \geq 0.999$) for a remarkable fraction of the possible $2 + 2$ quadruple systems. In turn, this may lead to stellar mergers, thereby forming hierarchical triples or producing blue stragglers (Perets & Fabrycky 2009), not to mention the possibility of the merger of two white dwarfs, producing a Type Ia supernova (SN) explosion (see the short summary regarding this question in Fang et al. 2018). Furthermore, a less extreme scenario can also be the formation of tight binaries (see e.g. Eggleton & Kiseleva-Eggleton 2001; Fabrycky & Tremaine 2007; Naoz & Fabrycky 2014).

Doubly eclipsing quadruples constitute a remarkable subclass of $2 + 2$ quadruple systems (and/or subsystems), where both inner binaries exhibit eclipses. The first known, and for some decades the sole representative, of these objects is the pair of W UMa-type eclipsing binaries (EBs) BV and BW Dra (Batten & Hardie 1965). The discovery of the second member of this group (V994 Her) was reported more than four decades later (Lee et al. 2008). During the last decade, however, due to the advent of the long duration, almost continuous photometric sky surveys, both ground-based [e.g. Wide Angle Search for Planets (SuperWASP), Pollacco et al. 2006; Optical Gravitational Lensing Experiment (OGLE), Pietrukowicz et al. 2013, etc.] and space photometry [especially *Kepler*, Borucki et al. 2010, and *Convection, Rotation and planetary Transits (CoRoT)* space telescopes, Auvergne et al. 2009], several new doubly eclipsing quadruple *candidates* have been discovered photometrically. Some examples, without any attempt at completeness, are KIC 4247791 (Lehmann et al. 2012), Cze V343 (Cagaš & Pejcha 2012), 1SWASP J093010.78+533859.5 (Lohr et al. 2015), EPICs 212651213 (Rappaport et al. 2016) and 220204960 (Rappaport et al. 2017). (Some of these quadruples have farther, more distant, and also likely bound companions as well.) Another, extraordinarily interesting system is KIC 4150611, which consists of three or four EBs, and one ‘binary’ of the double binary configuration is itself a triply eclipsing triple subsystem (Shibahashi & Kurtz 2012; Hełminiak et al. 2017). Additional blended EB light curves amongst CoRoT and *Kepler* targets were reported by Erikson et al. (2012), Fernández Fernández & Chou (2015), Hajdu et al. (2017), and Borkovits et al. (2016).

One should note, however, that by observing only a light curve that is characterized by the blended light of two EBs, one cannot be certain that the two EBs really form a gravitationally bound system. The small separation or even the unresolved nature of the optical images of the sources, as well as reasonably similar radial velocities and/or proper motions, can be very good indirect indicators of the bound nature of the pairs, but definitive evidence can be obtained only if the relative motion, or any other dynamical interactions of the two binaries, can be observed. Regarding these latter strict requirements, at this moment, to the best of our knowledge, there are only three pairs of EBs exhibiting blended light curves, for which their gravitationally bound, quadruple nature is beyond doubt. These are V994 Her (Zasche & Uhlař 2016), V482 Per (Torres et al. 2017) in which cases the light travel time effect (LTTE) was clearly detected, and EPIC 220204960 (Rappaport et al. 2017) that exhibits dynamically forced rapid apsidal motions in both binaries.²

In this work we report the discovery with NASA’s *Kepler Space Telescope* during Campaign 7 of its two-wheeled mission (hereafter referred to as K2) of a quite likely physically bound quadruple system consisting of two EBs, with orbital periods of 3.59470 and 0.61825 d. We derive many of the parameters for this system. The paper is organized as follows. In Section 2 we describe the 80-d K2 observation of EPIC 219217635 with its two physically associated EBs. We have obtained Keck adaptive optics (AO) imaging of the target star (see Section 3), and we find that the two binaries are unresolved down to ~ 0.05 arcsec. In Section 4 we discuss the eight eclipse minima that we were able to measure with ground-based photometry and analyse them together with the other eclipse minima determined from the 80-d-long K2 light curve in Section 5. We obtained 20 RV spectra that lead to mass functions for the two binaries; these are described in Section 6. We then use our improved light curve and RV curve emulator to model and evaluate both the EB light curves and the RV curves simultaneously (see Section 7). In Section 8 we explore the constraints we can place on the parameters of the outer quadruple orbit. In Section 9 we investigate the likely mass transfer evolution that has occurred in binary B. Finally, we summarize our findings and draw some conclusions in Section 10.

2 K2 OBSERVATIONS

As part of our ongoing search for EBs, we downloaded all available K2 extracted light curves common to Campaign 7 from the Mikulski Archive for Space Telescopes (MAST).³ We utilized both the Ames pipelined data set and that of Vanderburg & Johnson (2014). The flux data from all 24 000 targets were searched for periodicities via Fourier transforms and the Box-Least Squares (BLS) algorithm (Kovács, Zucker & Mazeh 2002). The folded light curves of targets with significant peaks in their fast Fourier transforms (FFTs) or BLS transforms were then examined by eye to look for unusual objects among those with periodic features. In addition, some of us (MHK, DLC, and TLJ) visually inspected all the K2 light curves for unusual stellar or planetary systems with `LCTOOLS` (Kipping et al. 2015).

Within a day after the release of the Field 7 data set, EPIC 219217635 was identified as a potential quadruple star system by both visual inspection and via the BLS algorithmic search. A 2-week-long section of the K2 light curve is shown in Fig. 1, where several features can be seen by inspection. The eclipses of the 3.595-d ‘A’ binary and 0.618-d ‘B’ binary are fairly obvious. Each binary has a deep and a shallow eclipse.

The disentangled and folded light curve of each binary is shown separately in Fig. 2. These plots demonstrate the likely semidetached nature of the 0.618-d binary and the detached nature of the 3.595-d binary.

We return to a more detailed quantitative analysis of the light curves of the two binaries in Section 7. To start, we simply collect the available photometry on the target-star image in Table 1. Note that these magnitudes refer to the combined light from all four stars in both binaries.

rapid eclipse depth variations, and therefore, probably inclination variations, and one of them also shows rapid apsidal motion. Thus, with high likelihood, this object is also a dynamically interactive, bound quadruple system.

³http://archive.stsci.edu/k2/data_search/search.php

²Most recently Hong et al. (2018) have published an analysis of two double EB candidates in the Large Magellanic Cloud, namely OGLE-LMC-ECL-15674 and OGLE-LMC-ECL-22159. The binaries in the first system exhibit

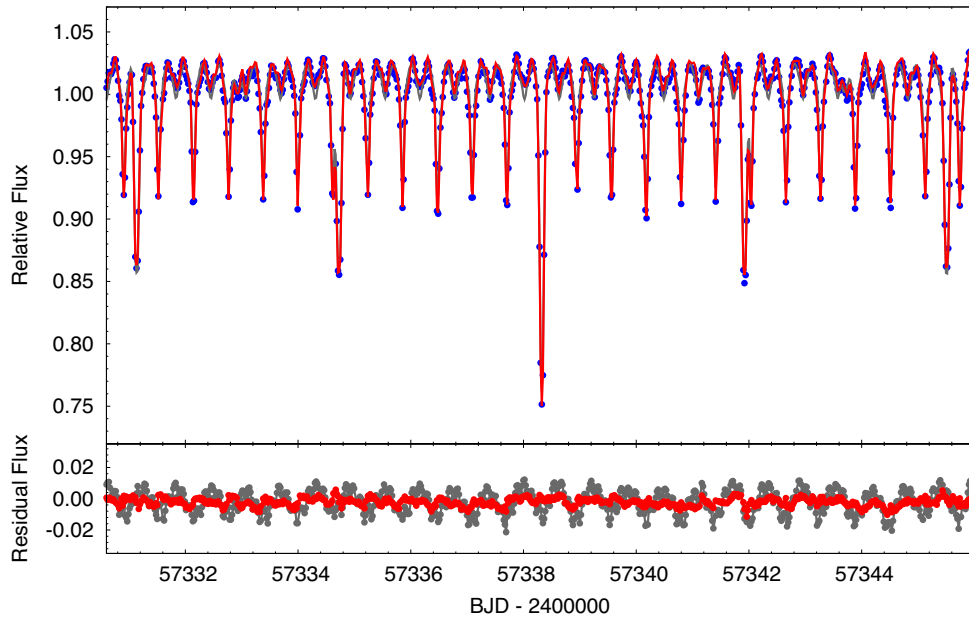


Figure 1. A zoomed-in ~ 14 -d segment of the K2 flux data showing the superposition of the eclipses of the A and B binaries. The data are shown in blue, the grey curve is a pure, double blended EB model fit, while the red curve is the net model fit taking into account both the binary and the other distortion effects (see text for details). The residuals of the data from the two models are shown in the bottom panel.

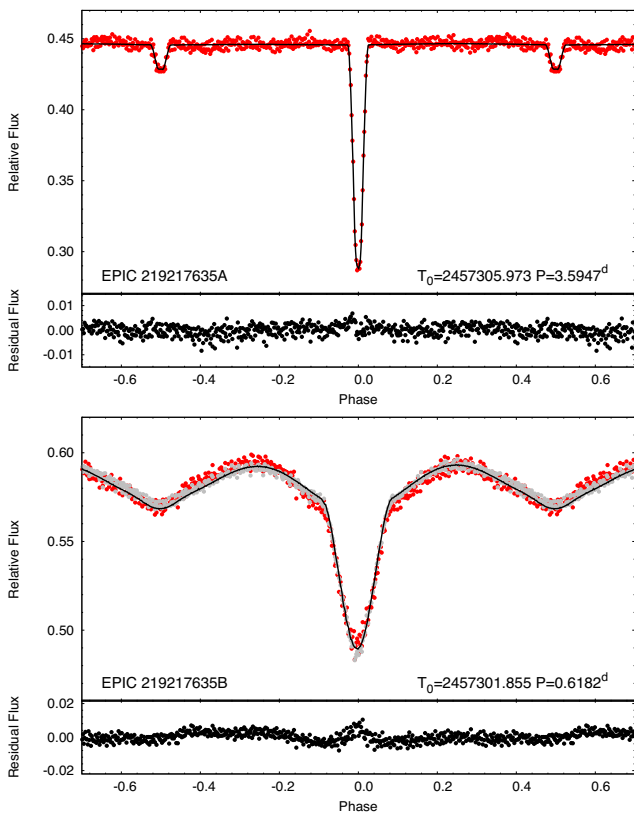


Figure 2. The disentangled and folded light curves of the 3.595-d ‘A’ binary and the 0.618-d ‘B’ binary (red dots). The black curves represent the disentangled, folded light curves, obtained from the simultaneous light-curve solution (partially shown in Fig. 1). In the case of binary B the grey dots represent the sum of the disentangled, folded light curve and a simple model of the rotational spot modulation (see text for details). The bottom panel for each binary shows the folded, disentangled residuals of the full K2 data from the model fit.

Table 1. Properties of the EPIC 219217635 system.

RA (J2000)	18:59:00.625
Dec. (J2000)	−17:15:57.13
K_p	12.72
B^b	13.86
g^a	13.42
V^b	13.13
R^b	11.74
r^a	12.72
z^a	13.42
i^b	12.43
J^c	11.44
H^c	11.11
K^c	11.02
$W1^d$	10.58
$W2^d$	10.61
$W3^d$	10.79
$W4^d$...
Distance (pc) ^e	870 ± 100
μ_α (mas yr ^{−1}) ^f	-1.9 ± 1.5
μ_δ (mas yr ^{−1}) ^f	-7.1 ± 2.4

^aTaken from the Sloan Digital Sky Survey (SDSS) image (Ahn et al. 2012). ^bFrom VizieR <http://vizier.u-strasbg.fr/>; Fourth U.S. Naval Observatory CCD Astrograph Catalog (UCAC4; Zacharias et al. 2013). ^cTwo Micron All Sky Survey (2MASS) catalogue (Skrutskie et al. 2006). ^dWide-field Infrared Survey Explorer (WISE) point source catalogue (Cutri et al. 2013). ^eBased on photometric parallax only (see Section 7). This utilized an adapted V magnitude of 13.1. ^fFrom UCAC4 (Zacharias et al. 2013; Smart & Nicastro 2014; Huber et al. 2016).

3 ADAPTIVE OPTICS IMAGING

We obtained Keck II/Near-Infrared Camera 2 (NIRC2; PI: Keith Matthews) observations of the target star EPIC 219217635 on 2017 May 10UT using the narrow camera (10×10 arcsec² field of view) to better characterize this quadruple system. Our observations used

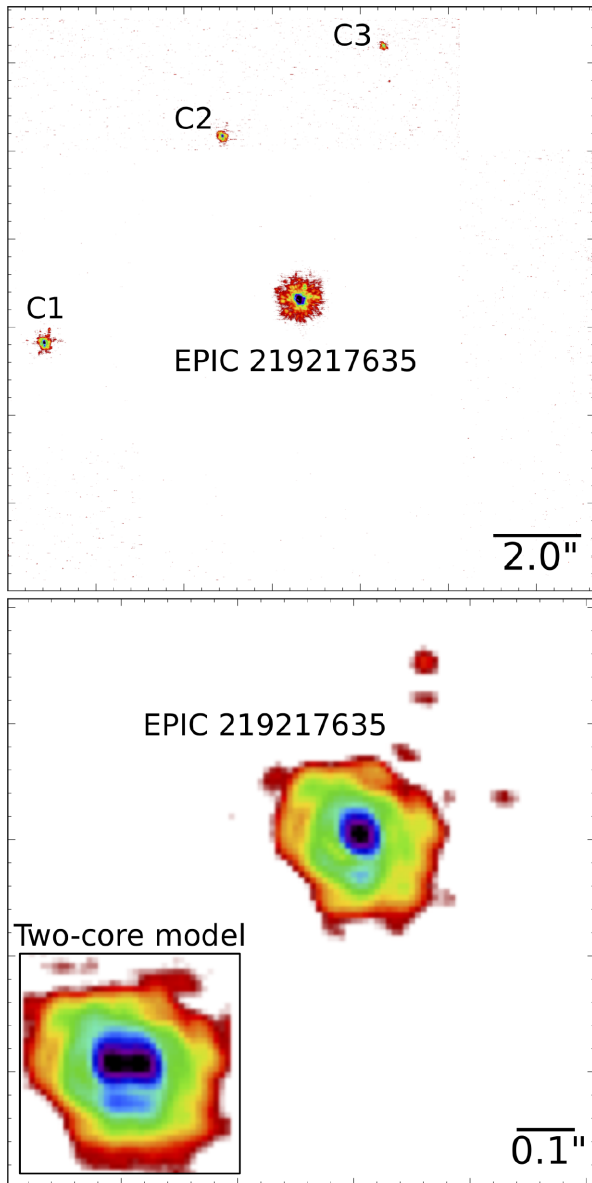


Figure 3. Keck AO image in K_s band of EPIC 219217635. Top panel: full image covering $\sim 13 \times 13$ arcsec². Three of the neighbouring stars are labelled C1, C2, and C3 for reference. Bottom panel: zoom-in around the target star EPIC 219217635. The inset shows a simple simulation of what the image would look like if the two binaries were separated by 0.05 arcsec (see text for a description of how this was generated). We conclude that the two binaries in this target image are clearly unresolved at the 0.05 arcsec level.

the target star as the guide star and dome flat-fields and dark frames to calibrate the images and remove artefacts.

We used a three-point dither pattern to acquire twelve 8-s frames of EPIC 219217635 in the K_s band (central wavelength 2.145 μm), for a total on-sky integration time of 96 s. Fig. 3 shows a stacked K_s band image of this target. The top panel shows the full AO image that covers 13×13 arcsec² on the sky, and includes three of the neighbour stars (labelled C1, C2, and C3), which are likely to be background stars rather than gravitationally bound companions. The AO photometry for the three nearby stars is given in Table 2. Because of the large separations of these neighbour stars, C1 only appears in two out of the three dither positions, while C2 and

Table 2. Stellar neighbours of EPIC 219217635^a.

Star	Flux ratio (K_s band)	Separation (mas)	Pos. angle (deg E of N)	t_{exp}^b (s)
C1	5.18 ± 0.11	5873 ± 2.9	99.53 ± 0.03	64
C2	11.49 ± 0.58	4087 ± 2.2	25.08 ± 0.03	32
C3	29.75 ± 0.74	6036 ± 3.0	341.39 ± 0.03	32

^aResults obtained from the Keck AO image. ^bTotal exposure time on each neighbour star. While the target star was present for the full 96 s of integration, the neighbour stars only appeared in-frame for a subset of the dither positions.

C3 appear in only one out of three dither positions. The K_s band astrometry was computed via point spread function (PSF) fitting using a combined Moffat and Gaussian PSF model following the techniques described in Ngo et al. (2015) and the NIRC2 narrow camera plate scale and distortion solution presented in Service et al. (2016).

In the bottom panel of Fig. 3, we show a zoomed-in image of the target star. This blown-up image looks distinctly single, and shows no sign of the core even being elongated. We have carried out simulations of close pairs of comparably bright images, at a range of spacings, and we conclude from this that separations between the two binaries of $\gtrsim 0.05$ arcsec can be conservatively ruled out. At a source distance of some 870 pc, this sets an upper limit on the projected physical separation of ~ 50 au.

A simple demonstration of what the AO image would look like if the two binaries (of nearly equal brightness; see Section 7) were separated by 0.05 arcsec in the horizontal direction is shown in the inset to the bottom panel in Fig. 3. To generate the inset figure, we simply duplicated the zoomed-in AO image, shifted it by 0.05 arcsec in the horizontal direction, and added it to the original image. One can see that if the two binaries were indeed separated by 0.05 arcsec, the core of the image would be noticeably elongated.

4 GROUND-BASED PHOTOMETRY

4.1 HAO observations

The Hereford Arizona Observatory (HAO) consists of a 0.34-m Meade brand Schmidt–Cassegrain Telescope (SCT) on a fork mount, inside an ExploraDome. All hardware is controlled via buried cables from a nearby residence. MAXIM DL 5.2 software is used to control the telescope, dome, focuser, filter wheel, and SBIG ST-10XME CCD camera. The unbinned image scale was 0.52 arcsec pixel⁻¹. All observations were made using a V -band filter, with exposure times of 60 s. Images were calibrated using master bias, dark and flat images. 10 reference stars and seven calibration stars were employed for converting instrument magnitude to V magnitude.

4.2 PEST observations

Perth Exoplanet Survey Telescope (PEST) is a home observatory with a 12-inch Meade LX200 SCT $f/10$ telescope with a SBIG ST-8XME CCD camera. The observatory is owned and operated by Thiam-Guan (TG) Tan. PEST is equipped with a $BVRI$ filter wheel, a focal reducer yielding $f/5$, and an Optec TCF-Si focuser controlled by the observatory computer. PEST has a 31×21 arcmin² field of view and a 1.2 arcsec pixel⁻¹ scale. PEST is located in a suburb of the city of Perth, Western Australia. PEST observed

EPIC 219217635 on 7 nights between 2017 June 5 and 2017 August 23 in the *V* band with 120-s integration times.

In all, the HAO and PEST observations led to measurements of four precise primary eclipse times for the 3.595-d ‘A’ binary and an equal number of primary eclipses for the 0.618-d ‘B’ binary (see the last column of Tables 3 and 4). Additionally, on the night of 2017 June 12 an event involving an overlapping primary eclipse of binary A and a secondary eclipse of binary B was also observed at PEST Observatory. However, due to the composite nature of this eclipse we were not able to determine the mid-eclipse times with satisfactory accuracies and, therefore, we did not tabulate this event.

5 PERIOD STUDY

In order to look for and analyse the possible eclipse timing variations (ETVs) in the two binaries, we determined the times of each eclipse minimum using the K2 data with the blended binaries in the following manner. First we formed a folded, binned light curve with the period of the 0.618-d binary B in such a way that the narrow region around the primary and secondary eclipses of the 3.595-d binary A was omitted. Then, the profile of the primary eclipse of this folded light curve (lower panel of Fig. 2) was used as a template for calculating the times of the primary eclipses of binary B in the K2 data set. (We decided not to utilize the secondary eclipses, due to the fact that they are rather shallow.)

In order to obtain the times of the primary eclipses of binary A, we removed the folded, binned, averaged binary B light curve from the K2 data set with the use of a three-point local Lagrange interpolation. Then, this disentangled light curve (upper panel of Fig. 2) was used both for forming the folded, binned, averaged light curve of binary A, and also for determining the times of the primary eclipses of binary A. (Here, for the same reasons as mentioned above, we utilized only the times of the primary eclipses.)

In such a way we obtained the first iteration K2 ETV curves for both binaries. Later, however, during our analysis, we realized that besides the classical binary light-curve variations, the light curve also exhibits some additional periodic variations (see Section 7). Thus, after the separation and removal of these extra periodic signals from the K2 light curve, we repeated the process described above, and we were able to refine the ETV curves (see Figs 4 and 5, and also Tables 3 and 4).

Furthermore, we have carried out ground-based photometric follow-up observations with two telescopes on 8 nights between 2017 May and August (see Section 4). We were thereby able to determine eight additional primary eclipse times (four for both binaries; given at the end of Tables 3 and 4), which made it possible to extend significantly the observing window and to check for longer time-scale trends in the period variations of the two binaries. In order to determine the ground-based eclipse times, we first converted these observations to the flux regime and then used the same K2 template eclipse profiles as before. Furthermore, in the case of the binary A eclipses we removed the ellipsoidal light variations (ELVs) of binary B via the use of the folded, disentangled binary B K2 light curve after phasing it according to its expected phase at the epoch of the ground-based observations.

Regarding the eclipse timings of binary A (Fig. 4) no definitive short-term ETVs can be seen during the 80 d of the K2 observations. The constant binary period is found to be $P_{A-K2} = 3^d59469 \pm 0^d00002$. On the other hand, the four ground-based eclipse times (which span a similar time interval) do not phase up to the K2 data. Fitting a constant period to the four ground-based data points yields $P_{A-2017} = 3^d59499 \pm 0^d00001$ that differs

by ~ 25.6 s from the K2 period (at the 12σ level). We also fit the joint K2 and 2017 ground-based data using a quadratic ephemeris (see black, dashed segments of the corresponding parabola in Fig. 4). A parabolic ETV represents a linear period variation during the 1.9-yr span of both sets of observations. As one can see, the parabolic fit is quite poor. The resultant period variation rate is found to be $\Delta P = 1.4 \pm 0.3 \times 10^{-6}$ d cycle $^{-1}$ or, $\dot{P}/P = 4.0 \pm 0.8 \times 10^{-5}$ yr $^{-1}$. Assuming that the source of this period variation was Keplerian orbital motion of the binary around the centre of mass of the quadruple system, one can convert this quantity into a variation in the systemic RV of binary A, as $\dot{\gamma}_A \approx c\Delta P/P^2$, which results in $\dot{\gamma}_A \simeq 0.038 \pm 0.008$ cm s $^{-2}$. As we find later, this value is an order of magnitude higher than we find directly from our RV study (see Section 6).

We turn now to the ETV curve for binary B (see Fig. 5). In this case the K2 data, after the removal of the non-binary light-curve variations, clearly reveal short-term, non-linear behaviour in the timing data. On the other hand, however, this non-linear trend, which would correspond to an increasing orbital period, obviously did not continue all the way to the time of the ground-based observations. These latter measurements are in conformity with a constant average period since the beginning of the K2 observations.

Speculating on the origin of these period variations, we can only state with certainty that none of them could arise from the orbit of the two binaries around each other. First, there is the evident contradiction between the period variations found in binary A and the directly measured value of $\dot{\gamma}_A$ found for binary A (see Section 6). Second, there is also the fact that, according to our combined RV and light-curve solution (see Section 7), the total mass of each of the two binaries is similar and, therefore, the ETVs arising from the orbits of the two binaries forming the quadruple system should be similar in amplitude and opposite in phase.⁴ In the case of binary B, the spotted nature of at least one of the stars might offer a plausible explanation for the observed short-term ETVs, as similar behaviour has been reported for several spotted *Kepler* binaries (see e.g. Tran et al. 2013; Balaji et al. 2015).

In the case of binary A, an interpretation of the observed ETV behaviour will require further observations.

6 NOT-FIES RADIAL VELOCITY STUDY

We obtained 20 spectra of EPIC 219217635 employing the Nordic Optical Telescope (NOT) and its Fibre-fed Echelle Spectrograph (FIES; Frandsen & Lindberg 1999; Telting et al. 2014) in high-resolution mode ($R \sim 67\,000$). The spectra have been taken between 2016 May 18 and 2017 July 5 with exposure times ranging between 20 and 35 min. Each science exposure was accompanied by one ThAr exposure immediately prior to wavelength calibration.

The data reduction was carried out using FISTOOL.⁵ In the following we used the wavelength-calibrated extracted, but not order-merged spectra. Cosmic rays have been identified and removed, the blaze function of the spectrograph was accounted for using flat-field exposures, and the spectra have been normalized. For the purpose of obtaining RVs we focus on the spectral region between 4500 and 6700 Å. At shorter wavelengths the typical signal-to-noise ratio (S/N) per spectral bin is below 3 for the combined spectrum of the two binaries. At longer wavelengths few stellar lines are present.

⁴Strictly speaking this is only true for the LTTE. The dynamical contribution to the ETVs would differ due to the different periods of the two inner binaries.

⁵<http://www.not.iac.es/instruments/fies/fiestool/>

Table 3. Mid-times of primary eclipses of EPIC 219217635A.

BJD – 240 0000	Cycle no.	Std. dev. (d)	BJD – 240 0000	Cycle no.	Std. dev. (d)	BJD – 240 0000	Cycle no.	Std. dev. (d)
57302.37640	–1.0	0.00057	57334.73057	8.0	0.00012	57367.08298	17.0	0.00129
57305.97293	0.0	0.00014	57338.32397	9.0	0.00022	57370.67604	18.0	0.00019
57309.56653	1.0	0.00018	57341.92041	10.0	0.00016	57374.27121	19.0	0.00019
57313.16229	2.0	0.00019	57345.51450	11.0	0.00017	57377.86827	20.0	0.00173
57316.75708	3.0	0.00020	57349.10967	12.0	0.00017	57381.46098	21.0	0.00012
57320.35134	4.0	0.00019	57352.70271	13.0	0.00046	57891.91419	163.0	0.00009
57323.94668	5.0	0.00022	57356.29934	14.0	0.00031	57924.26923	172.0	0.00010
57327.54058	6.0	0.00018	57359.89390	15.0	0.00011	57942.24434	177.0	0.00020
57331.13552	7.0	0.00039	57363.48917	16.0	0.00022	57988.97864	190.0	0.00025

Note. Most of the eclipses (cycle nos –1 to 21) were observed by *Kepler* spacecraft. Last four eclipses (under the horizontal line) were observed at HAO (no. 163) and PEST (nos 172–190) observatories.

Table 4. Mid-times of primary eclipses of EPIC 219217635B.

BJD – 240 0000	Cycle no.	Std. dev. (d)	BJD – 240 0000	Cycle no.	Std. dev. (d)	BJD – 240 0000	Cycle no.	Std. dev. (d)
57301.85339	0.0	0.00055	57329.67001	45.0	0.00027	57357.49055	90.0	0.00043
57303.08879	2.0	0.00020	57330.28886	46.0	0.00107	57358.72688	92.0	0.00047
57303.70704	3.0	0.00045	57330.90695	47.0	0.00022	57359.34632	93.0	0.00036
57304.32550	4.0	0.00027	57331.52407	48.0	0.00039	57360.58266	95.0	0.00050
57304.94365	5.0	0.00027	57332.14301	49.0	0.00007	57361.20038	96.0	0.00012
57305.56253	6.0	0.00152	57332.76132	50.0	0.00025	57362.43609	98.0	0.00067
57306.18046	7.0	0.00003	57333.37931	51.0	0.00083	57363.05545	99.0	0.00047
57306.79734	8.0	0.00071	57333.99694	52.0	0.00061	57363.67455	100.0	0.00061
57307.41647	9.0	0.00048	57334.61525	53.0	0.00014	57364.29122	101.0	0.00017
57308.03398	10.0	0.00091	57335.23419	54.0	0.00078	57364.91057	102.0	0.00114
57308.65247	11.0	0.00076	57335.85254	55.0	0.00026	57365.52781	103.0	0.00080
57309.27014	12.0	0.00022	57337.08857	57.0	0.00031	57366.14836	104.0	0.00045
57309.88869	13.0	0.00108	57337.70643	58.0	0.00032	57366.76422	105.0	0.00031
57310.50691	14.0	0.00012	57338.94273	60.0	0.00006	57367.38405	106.0	0.00077
57311.12496	15.0	0.00055	57339.56161	61.0	0.00011	57368.00177	107.0	0.00084
57311.74309	16.0	0.00007	57340.79859	63.0	0.00075	57368.62095	108.0	0.00047
57312.36134	17.0	0.00009	57342.03502	65.0	0.00036	57369.23842	109.0	0.00038
57312.97808	18.0	0.00032	57342.65434	66.0	0.00089	57369.85815	110.0	0.00200
57313.59722	19.0	0.00026	57343.27132	67.0	0.00023	57370.47323	111.0	0.00026
57314.21555	20.0	0.00036	57343.89018	68.0	0.00025	57371.09366	112.0	0.00041
57314.83386	21.0	0.00009	57344.50773	69.0	0.00024	57371.71162	113.0	0.00039
57315.45107	22.0	0.00316	57345.12682	70.0	0.00090	57372.33037	114.0	0.00067
57316.07058	23.0	0.00034	57345.74510	71.0	0.00041	57372.94706	115.0	0.00044
57317.30683	25.0	0.00010	57346.36355	72.0	0.00078	57373.56618	116.0	0.00028
57317.92490	26.0	0.00070	57346.98041	73.0	0.00011	57374.80215	118.0	0.00045
57319.16173	28.0	0.00057	57347.59947	74.0	0.00042	57375.41912	119.0	0.00070
57321.01640	31.0	0.00040	57348.21883	75.0	0.00107	57376.65586	121.0	0.00086
57321.63400	32.0	0.00006	57348.83568	76.0	0.00023	57377.27327	122.0	0.00047
57322.87125	34.0	0.00014	57349.45359	77.0	0.00013	57378.51223	124.0	0.00009
57323.48879	35.0	0.00046	57350.07298	78.0	0.00040	57379.12853	125.0	0.00041
57324.10676	36.0	0.00063	57350.69137	79.0	0.00037	57380.36682	127.0	0.00074
57324.72549	37.0	0.00035	57351.30971	80.0	0.00014	57380.98310	128.0	0.00066
57325.34337	38.0	0.00029	57351.92734	81.0	0.00137	57381.60127	129.0	0.00047
57325.96183	39.0	0.00059	57352.54397	82.0	0.00022	57382.21900	130.0	0.00029
57326.57965	40.0	0.00053	57353.78200	84.0	0.00037	57910.16115	984.0	0.00013
57327.19787	41.0	0.00034	57355.01923	86.0	0.00029	57923.14305	1005.0	0.00015
57327.81569	42.0	0.00039	57355.63804	87.0	0.00178	57924.38240	1007.0	0.00023
57328.43373	43.0	0.00034	57356.87288	89.0	0.00035	57929.32426	1015.0	0.00013
57329.05172	44.0	0.00054						

Note. Most of the eclipses (cycle nos 0–130) were observed by *Kepler* spacecraft. Last four eclipses (under the horizontal line) were observed at the PEST Observatory.

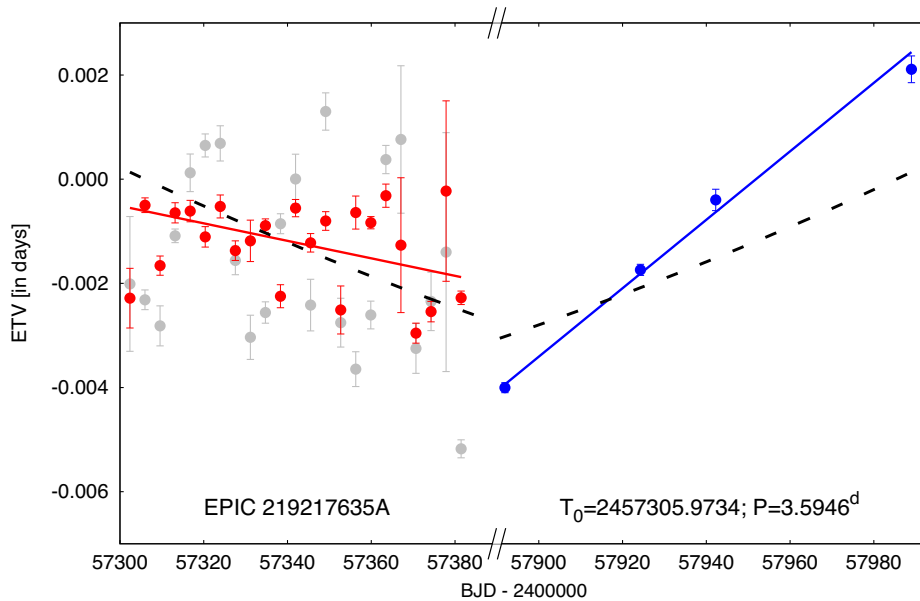


Figure 4. ETVs of binary A. Grey and red circles represent eclipse times determined from the K2 observations before and after the removal of non-binary light-curve variations, respectively. Blue data points represent the ground-based timing measurements. Red and blue lines are linear fits to the red and blue ETV points, respectively, which would illustrate two constant-period segments with a period difference of 26 s (note in particular the broken time axis). Black dashed lines illustrate the two sections of a parabola that result from a quadratic fit to the red and blue ETV points together, i.e. modelling a constant rate of increase in the orbital period.

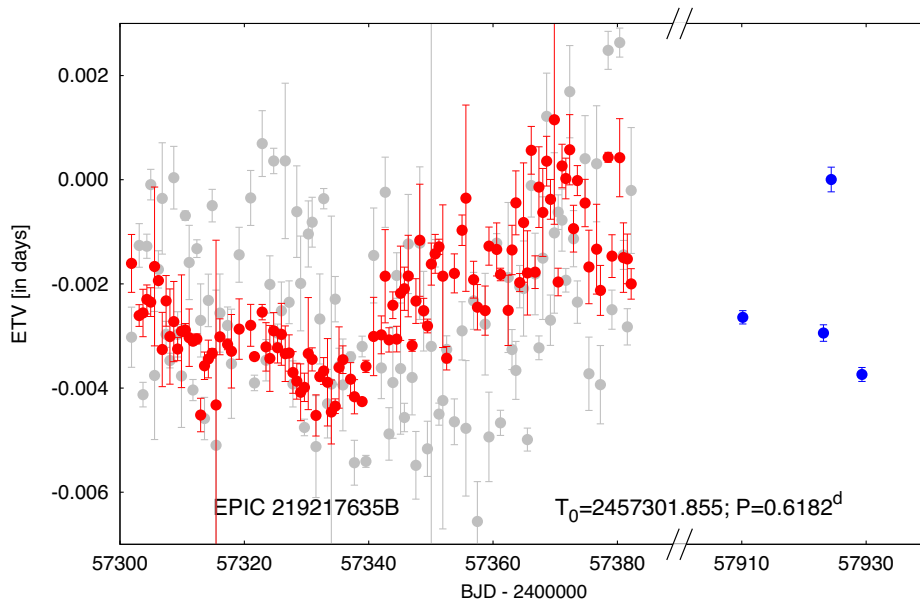


Figure 5. ETVs of binary B. Grey and red circles represent eclipse times determined from the K2 observations before and after the removal of light-curve variations, respectively, that are not inherent to the binary light curve. Blue data points represent the ground-based timing measurements. Note the broken time axis between the two sets of observations.

We created cross-correlation functions (CCFs) for each spectral order of each observation using a template obtained from the PHOENIX library (Husser et al. 2013). Specifically we used the PHOENIX model with $T_{\text{eff}} = 6500$ K, $\log g = 4.0$, and solar metallicity. We checked if using different templates with somewhat different parameters changes the RV we derive (see below), which is not the case.

Next we fitted two Gaussians to the CCF of each observation obtained by simple summation of all CCFs from the different orders. One Gaussian has a small σ of 11 km s^{-1} representing the primary

from binary A. The second Gaussian with $\sigma = 120 \text{ km s}^{-1}$ represents the primary from binary B. The positions of these Gaussians are interpreted as RVs of the two primary components. We estimate the uncertainties in these RVs using the following approach. The CCFs from the different spectral orders are grouped into four different wavelength regions. RVs for each of the four different orders are obtained in the same way as for the CCFs from the complete spectral region and the standard deviation about the mean is used as the RV uncertainty.

The RV plots obtained with the NOT-FIES spectrometer are shown in Fig. 6, and the individual RV measurements are listed in Table 5. The RV curve for the primary star in binary A (top panel) has very well determined parameter values with a typical uncertainty per RV point of $\sim 0.5 \text{ km s}^{-1}$. The orbital amplitude, K_A , is $61.28 \pm 0.15 \text{ km s}^{-1}$, while the system velocity is $\gamma_A = 30.91 \pm 0.13 \text{ km s}^{-1}$. For the primary component in binary B (bottom panel), the typical uncertainties per RV point are $\sim 12 \text{ km s}^{-1}$. The corresponding elements are $K_B = 64.1 \pm 3.6 \text{ km s}^{-1}$ and $\gamma_B = 32.3 \pm 2.2 \text{ km s}^{-1}$. These were all for assumed circular orbits, but we fit for, and set constraints on, eccentric orbits as well.

We also used the NOT-FIES spectral data to determine some of the properties of the primary star in binary A. The results are given in Table 5 and shown in Fig. 7. After obtaining RVs for the A and B binaries we use the tomography algorithm developed by Bagnuolo & Gies (1991) to separate the spectra. We stack the separated spectra to obtain co-added, high S/N spectra of the A and B binaries. We derive stellar parameters of star A1 from the co-added spectrum. Within the spectroscopic framework iSpec (Blanco-Cuaresma et al. 2014), we fit synthetic spectra computed using SPECTRUM (Gray & Corbally 1994) and ATLAS9 atmospheres (Castelli & Kurucz 2004) to the wavelength region 5000–5500 Å. The spectroscopically determined parameters are listed in Table 5. We derive the stellar mass, radius, and age by fitting spectroscopic constraints (T_{eff} , $\log g$, [Fe/H]) to a grid of a Bag of Stellar Tracks and Isochrones (BaSTI) isochrones (Pietrinferni et al. 2004) using the Bayesian Stellar Algorithm (bast.a; Silva Aguirre et al. 2015), see Table 5.

In Fig. 7, we show the location (with uncertainties) of star A1 in the $\log g - T_{\text{eff}}$ plane. Superposed on the plot are evolution tracks for stars of mass 0.9–1.5 M_{\odot} (mass increases from left to right) in steps of 0.1 M_{\odot} . Moreover, the tracks are colour coded according to the isochrones of stellar evolution time.

The lines of the primary star in binary B were too broad ($v \sin i \approx 120 \text{ km s}^{-1}$) to allow for a similar analysis.

7 SIMULTANEOUS LIGHT-CURVE AND RV-CURVE MODELLING

We carried out a simultaneous analysis of the blended light curves of the two EBs, and the two radial velocity curves of the primaries of the two EBs using our light-curve emulator code `lightcurve-factory` (Borkovits et al. 2013; Rappaport et al. 2017). This code employs a Markov chain Monte Carlo (MCMC)-based parameter search, using our own implementation of the generic Metropolis–Hastings algorithm (see e.g. Ford 2005). The basic approach and steps for this study are similar to that which was followed during the previous analysis of the quadruple system EPIC 220204960, described in Rappaport et al. (2017, section 7). Therefore, here we concentrate mainly on the differences compared to this previous work.

7.1 New features of the analysis

First, for a more accurate modelling of the strong ELV effect in the light curve of binary B (see Fig. 2), we implemented the Roche-equipotential-based stellar surface calculations into our code (see e.g. Kopal 1989; and Avni 1976; Wilson 1979, for a formal extension to eccentric orbits and asynchronous stellar rotation). Furthermore, we included an additional switch in the code to set the size parameter of one star (or both) so that it would exactly fill its Roche lobe. In

such a way we were able to model the semidetached configuration of binary B.

Second, because our code is now able to fit light-curve photometry, RV, and ETV curves at the same time, we decided to simultaneously analyse the two RV curves along with the blended light curve.

Third, after subtracting off the initial model light curves from the data set, we realized that the fluctuations in the residual light curve exhibit some distinct periodicities (Fig. 1, lower panel) with three dominant frequencies that are listed in Table 6. We fold the residual light curve about the two most significant periods, and plot the two folds separately in the panels of Fig. 8. Irrespective of their origin, these variations are modelled in the code in the following automated manner. In each trial step, after the removal of the blended EB model light curves from the observed data, the mathematical description of the residual curve is modelled by a harmonic function of the form

$$\Delta \mathcal{L} = \sum_{i=1}^3 a_i \sin(2\pi f_i t) + b_i \cos(2\pi f_i t), \quad (1)$$

where the f_i s are the given fixed frequencies, and the coefficients a_i and b_i are calculated by a linear least-squares fit. Then, this mathematical model of the residual light curve is added to the binary model light curve and the actual χ^2 value is calculated for this mixed model light curve.

7.2 Significance of the simultaneous analysis

The main significance of this simultaneous treatment is the following. Apart from the mass, m_{A1} , and the effective temperature, T_{A1} , of the primary of binary A, all the other astrophysically important parameters of both binaries can be obtained from the same analysis, at least in principle. To prove this statement one needs only recall that both binaries are single-lined spectroscopic binaries (i.e. SB1 systems), and it then follows that the amplitudes of the RV curves give the spectroscopic mass functions:

$$f(m_2) = \frac{(a_1 \sin i_1)^3 4\pi^2}{P^2 G} = \frac{m_2^3 \sin^3 i}{(m_1 + m_2)^2} = m_1 \frac{q^3 \sin^3 i}{(1+q)^2}. \quad (2)$$

Therefore, in the case of binary A, we can use the orbital inclination, i_A , obtained from the blended light-curve solution, to find the unknown mass m_{A2} , if we knew m_{A1} . On the other hand, for binary B, which we found to be a semidetached system, it is expected that its mass ratio, q_B , should be relatively well determined from the light-curve solution (Terrell & Wilson 2005). Therefore, by combining the spectroscopic mass function, $f(m_2)_B$, with the mass ratio, q_B , and the inclination angle, i_B , again both obtained from the blended light-curve solution, one can also calculate the individual masses of the two stars in binary B.

Furthermore, we also wish to point out that the joint photometric analysis of the two binaries inherently carries some information about the mass ratio of the two binaries and the temperature ratio of the primary star in each binary (T_{A1}/T_{B1}). Since it turns out that there is already sufficient information to adequately determine all the masses in the system, this means that equation (A3) effectively yields T_{A1}/T_{B1} . Therefore, if T_{A1} is known, one can also find T_{B1} and then, naturally, the effective temperatures of all four stars can also be obtained. Since it is conceptually interesting that the photometry does encode combined information about the mass ratio of the two binaries and T_{A1}/T_{B1} , we provide a brief discussion of this in Appendix A.

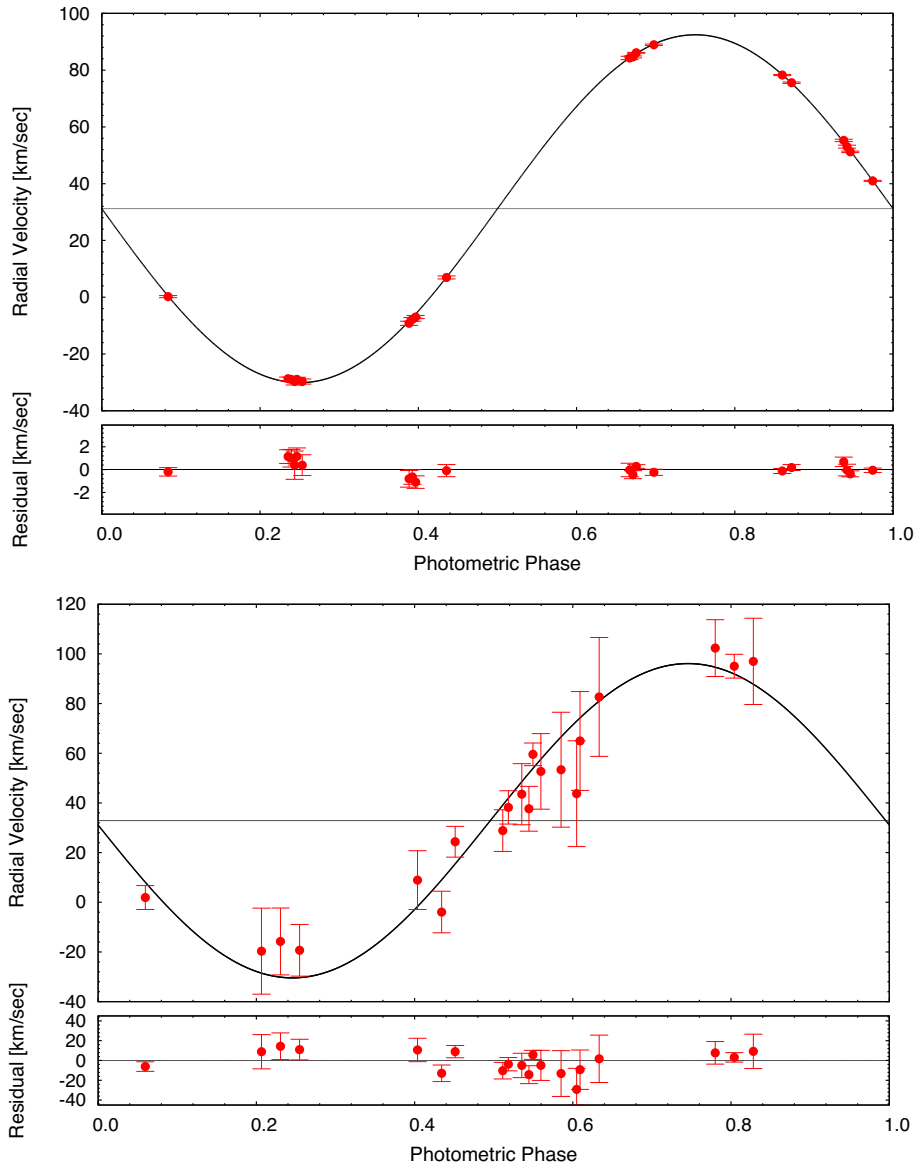


Figure 6. Folded RV curves for the 3.595-d ‘A’ binary (top panel) and the 0.618-d ‘B’ binary (bottom panel). The black curves are the best-fitting circular orbit models. For a better visualization all the individual observed and model data points are corrected for the non-zero $\dot{\gamma}$ values, i.e. we plot the $v_{\text{corr}} = v_{\text{obs/mod}} - \dot{\gamma}(t_{\text{obs/mod}} - t_0)$ data.

7.3 Fitted parameters and assumptions

As discussed above, all of the astrophysically important parameters of both binaries can be obtained from the same simultaneous analysis, except for the mass, m_{A1} , and the effective temperature, T_{A1} , of the primary of binary A. However, because T_{A1} and its uncertainty are directly known from the spectroscopic analysis, the only remaining task is to find one additional reasonable constraint to close the system of equations. As a good approximation for m_{A1} we use the value and uncertainty for m_{A1} obtained indirectly from the spectroscopic data, as was described in Section 6.

Turning now to the practical implementation of the combined analysis, we note that in most of the runs we adjusted 20–22 parameters. These are as follows.

(i) 2×3 orbital parameters: the two periods ($P_{A,B}$), inclinations ($i_{A,B}$), and reference primary eclipse times ($T_{0,A,B}$). (Note, in some

runs we allowed for an eccentric orbit in binary A and, therefore, the eccentricity, e_A , and argument of periastron, ω_A , of binary A were also adjusted, but we did not detect any significant, non-zero eccentricity. Thus, for most of the runs we simply adopted circular orbits for both binaries.)

(ii) 2×3 additional RV curve related parameters: systemic radial velocities ($\gamma_{A,B}$) and linear accelerations ($\dot{\gamma}_{A,B}$),⁶ and spectroscopic mass functions ($f(m_2)_{A,B}$).

(iii) The light-curve related parameters: temperature ratios (T_2/T_1)_{A,B} and also T_{B1}/T_{A1} ; the duration of the primary minima (Δt_{pri})_{A,B} (see Rappaport et al. 2017, section 7 for an explanation); the ratio of stellar radii in binary A (R_2/R_1)_A; and the extra light (l_x).

⁶Strictly speaking, this latter quantity was taken into account in a slightly unphysical manner; in particular, it was taken to be an absolutely independent variable, and it was not connected to any variation of the eclipsing period.

Table 5. Radial velocity study^a.

	Binary A	Binary B
RV measurements		
BJD – 240 0000	km s ⁻¹	km s ⁻¹
57526.6406	-9.40 ± 0.73	+55.8 ± 23
57526.6554	-8.01 ± 0.64	+67.3 ± 20
57526.6703	-7.20 ± 0.55	+85.1 ± 24
57527.6428	+84.09 ± 0.59	-17.3 ± 17
57527.6576	+84.45 ± 0.35	-13.4 ± 13
57527.6725	+85.91 ± 0.16	-17.0 ± 10
57528.6155	+55.04 ± 0.41	+104.7 ± 11
57528.6303	+52.84 ± 0.51	+97.4 ± 5
57528.6452	+51.01 ± 0.26	+99.3 ± 17
57529.6858	-28.91 ± 0.60	+31.2 ± 8
57529.7006	-29.18 ± 0.77	+45.8 ± 12
57529.7155	-29.87 ± 1.24	+55.0 ± 15
57666.3547	-29.62 ± 0.91	+42.7 ± 21
57669.3399	+0.31 ± 0.37	-5.0 ± 8
57682.3316	+89.05 ± 0.27	+23.0 ± 6
57683.3258	+41.12 ± 0.19	+0.53 ± 5
57864.7275	+7.46 ± 0.53	+32.5 ± 7
57916.5810	+78.88 ± 0.22	+1.94 ± 12
57934.5976	+76.21 ± 0.26	+52.1 ± 5
57939.5396	-28.29 ± 0.75	+30.1 ± 9
Orbit fits		
T_0 (BJD) ^b	245 7625.9007 ± 0.0012	245 7625.801 ± 0.005
P (d)	3.59486(4)	0.61815(2)
K (km s ⁻¹)	61.28 ± 0.15	64.1 ± 3.6
γ (km s ⁻¹)	+30.91 ± 0.13	+32.3 ± 2.2
e	≤ 0.01	...
$\dot{\gamma}$ (cm s ⁻²) ^c	0.0024 ± 0.0007	-0.020 ± 0.014
Spectroscopic parameters ^d		
T_{eff} (K)	6421 ± 134	...
log g (cgs)	4.15 ± 0.16 ^e	...
Fe/H (dex)	-0.03 ± 0.07	...
$v \sin i$ (km s ⁻¹)	16.7 ± 1	...
M_{A1} (M_{\odot})	1.23 ^{+0.10} _{-0.08}	...
R_{A1} (R_{\odot})	1.39 ^{+0.31} _{-0.17}	...
Age (Gyr)	2.4 ± 1	...

^aCarried out with the NOT-FIES spectrometer. ^bTime of the primary eclipse and reference time for P and K . ^cParameter fitted to the unfolded RV data set. ^dParameters refer to the primary star that contributes $\gtrsim 90$ per cent of the light from the A binary. ^eDerived from the summed spectra; see Section 6.

(iv) The mass ratio (q_B) of binary B.

(v) Finally, the effective temperature, T_{A1} , and mass, m_{A1} , of the primary of binary A, for which we incorporated Gaussian prior distributions with the mean and standard error set to the values obtained from the spectroscopic solution.

Regarding other parameters, a logarithmic limb darkening law was applied, for which the coefficients were interpolated from the passband-dependent pre-computed tables of the *phoebe* software⁷ (Prša & Zwitter 2005). Note that these tables are based on the stellar atmospheric models of Castelli & Kurucz (2004). The gravity darkening exponents were set to their traditional values appropriate for such late-type stars ($g = 0.32$). We found that the illumination/irradiation effect was negligible for the wider binary A; therefore, in order to save computing time, it was calculated only for the narrower binary B. The Doppler boosting effect was taken into account for both binaries (Loeb & Gaudi 2003; van Kerkwijk et al. 2011).

Furthermore, we assumed that all four stars rotate synchronously with their respective orbits. For the semidetached component of binary B this assumption seems quite natural. On the other hand, some primaries of semidetached systems have been found to be rapid rotators relative to their orbits (see e.g. Wilson 1994, for a review). In our case, however, we may reasonably assume that the highest amplitude peak in the residual light curve (see Table 6 and Fig. 8), with a period that differs by only ~ 5 –6 min from the orbital period of binary B, has its origin in the rotational modulation of the primary of binary B, which clearly dominates the light contribution of this binary. Thus, it is also reasonable to adopt a synchronous rotation for the primary of binary B. Regarding the detached binary A, the spectroscopically obtained projected rotational velocity of the primary component $v \sin i = 16.7 \pm 1$ km s⁻¹ (see Table 5) offers an a posteriori verification of our assumption since the projected synchronous rotational velocity that can be deduced from our solution is found to be in essentially perfect agreement with this result (see in Table 7, below). Finally, note that we have no information on the rotation of the secondary component of binary A but, due to its small contribution to the total flux of the system, its rotational properties have only a minor influence on our solution.

⁷<http://phoebe-project.org/1.0>

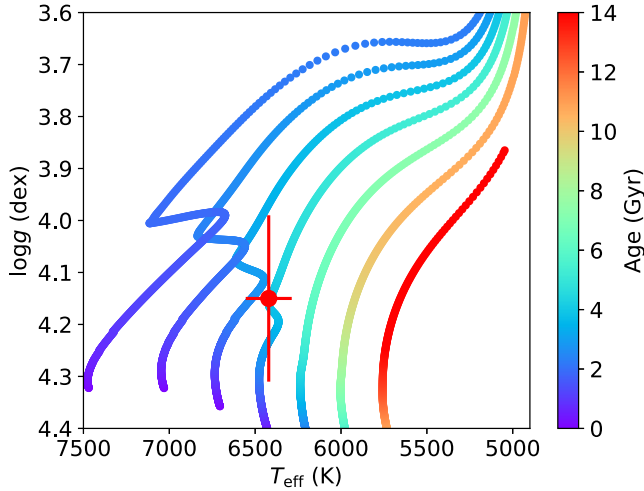


Figure 7. The spectroscopically determined location (with uncertainties) of star A1 in the $\log g - T_{\text{eff}}$ plane. The coloured curves are evolution tracks for stars of mass $0.9 - 1.5 M_{\odot}$ (increasing from left to right) in steps of $0.1 M_{\odot}$. Tracks are colour coded according to the isochrones of stellar evolution time. See text for details.

Table 6. The five most significant peaks of the period analysis of the residual light curve.

	Frequency (d^{-1})	Amplitude ($\times P_B$)	Amplitude ($\times 10^{-3}$ flux)	Phase (rad)
f_1^a	1.628417(1)	1.00669	7.520(1)	-1.2098
f_2^a	7.586925(1)	4.69175	3.217(1)	-1.2443
f_3^a	3.257062(1)	2.01352	2.128(1)	-0.1286
f_4	6.102445(1)	3.77375	1.784(1)	-2.7261
f_5	18.119794(1)	11.20528	1.352(1)	-0.8596

^aThe frequencies used for the light-curve fitting process.

7.4 Results of the simultaneous analysis

The orbital elements of the two binaries, and the astrophysically relevant parameters of the four stars, together with their uncertainties, are tabulated in Table 7. About half of these quantities were obtained directly from our simultaneous MCMC analysis of the photometric and RV data, while the others were calculated from the MCMC adjusted parameters using the relations discussed above, as well as some additional trivial ones. Examples of the latter include the calculation of the semimajor axes from the stellar masses and periods, and the determination of the volume-equivalent physical radii of the four stars from their fractional radii.

We also computed the luminosities of the four stars both in solar luminosity (L_{\odot}) and as bolometric absolute magnitudes. We also compute the total absolute visual magnitude (M_V)_{tot} of the quadruple system as a whole. For this latter quantity, the bolometric correction for each star was calculated with the formulae of Flower (1996).⁸ Furthermore, for the calculation of (M_V)_{tot} we assumed that the extra light contribution ($I_x = 0.048 \pm 0.030$) found in our light-curve solution from the *Kepler* photometric band is essentially the same as the contaminating light in *V* band. (However, since it appears that the extra light is fairly negligible, this issue is not

⁸The original coefficients listed in Flower (1996) contained typos that were corrected by Torres (2010). Naturally, these corrected coefficients were used in this work.

very important.) These luminosities and magnitudes are reported in Table 7.

Then, by the use of the observed *V* magnitude, listed in Table 1, we can estimate a photometric distance to the system. We first calculate the maximum hydrogen column density between us and the quadruple, N_{H} , using NASA’s High Energy Astrophysics Science Archive Research Center (HEASARC) on-line tools⁹ and find $N_{\text{H}} \lesssim 1.4 \times 10^{21} \text{ cm}^{-2}$. We then used a conversion from N_{H} to A_V taken from Guver & Özel (2009): $N_{\text{H}} \simeq 2.2 \times 10^{21} A_V$. This yields an extinction of $A_V \lesssim 0.63$. We also utilized a web-based applet¹⁰ to estimate $E(B - V) = 0.22 \pm 0.03$ that we translate to $A_V = 0.68 \pm 0.09$. When we propagate the associated uncertainties in all the involved quantities, we find a distance of $870 \pm 100 \text{ pc}$; this is also tabulated in the last row of Table 7.¹¹

A comparison of those astrophysical parameters of the *primary* star in binary A that were obtained both from the spectroscopic (Table 5), and the combined photometric + RV (Table 7) analysis shows slight but significant discrepancies. In particular, the radius inferred from the joint photometric + RV analysis ($R_{\text{A1}}^{\text{phot}} \simeq 1.19 \pm 0.03 R_{\odot}$) is $1.2\sigma_{\text{spec}}$ smaller than the spectroscopically inferred radius ($R_{\text{A1}}^{\text{spec}} \simeq 1.39^{+0.31}_{-0.17} R_{\odot}$). This leads to an RV + photometric $\log g_{\text{A1}}$ that is 0.22 ± 0.16 dex higher than that determined from the spectroscopic analysis.

This slight inconsistency in $\log g_{\text{A1}}$ should be considered together with the inferred absolute dimensions of the *secondary* component of binary A. While the effective temperature ($T_{\text{A2}} \simeq 4400 \pm 100 \text{ K}$) and mass ($m_{\text{A2}} \simeq 0.68 \pm 0.03 M_{\odot}$) of the secondary are in accord with the main-sequence nature of this star to within the 1σ uncertainty, the inferred stellar radius ($R_{\text{A2}} \simeq 0.74 \pm 0.02 R_{\odot}$) reveals a significantly oversized star for its mass. One might imagine that the inconsistency could readily be resolved assuming that the joint analysis failed to obtain the correct value for the ratio of the relative radii of binary A (r_2/r_1), which itself was an adjusted parameter. However, we note that the eclipses in binary A were found to be total (i.e. in the sense of four contact points) and, therefore, in this case the ratio of the stellar radii is relatively well determined. This discrepancy did lead us to conduct some further tests, initiating new MCMC runs in which the radius of the secondary of binary A was constrained with the use of the Tout et al. (1996) mass–radius relation. These runs led to significantly worse fits. In particular, that part of the χ^2 sum that was calculated exclusively from the light-curve solution was found to be higher by about $\approx 8 - 10$ per cent in the case of the solutions using a constrained secondary radius. Thus, using all the presently available information on the quadruple, we are able to resolve these discrepancies, but we believe that they are reasonable given the very different inputs, uncertainties, and analyses involved.

Binary B is found to be the more interesting of the two binaries from the perspective of stellar evolution theory. The stellar compo-

⁹<https://heasarc.gsfc.nasa.gov/docs/tools.html>

¹⁰<http://argonaut.skymaps.info/query?>

¹¹After this work was completed, the *Gaia* DR2 (Lindegren et al. 2018) was released that provides a distance to EPIC 219217635 of $588 \pm 17 \text{ pc}$. This is closer than the photometric distance we estimate of $870 \pm 100 \text{ pc}$, i.e. based on an approximate extinction of $A_V \simeq 0.65 \pm 0.09$. In order for the two distances to be reconciled would require either $A_V \simeq 1.5$ or an unrealistic adjustment of the system M_V that we infer from our joint RV and photometric analysis. Another, possibly more likely explanation would be if the finite separation of two binaries on the sky, i.e. $\lesssim 0.05$ arcsec causes the parallactic distance to be adversely affected (Szabados 1997).

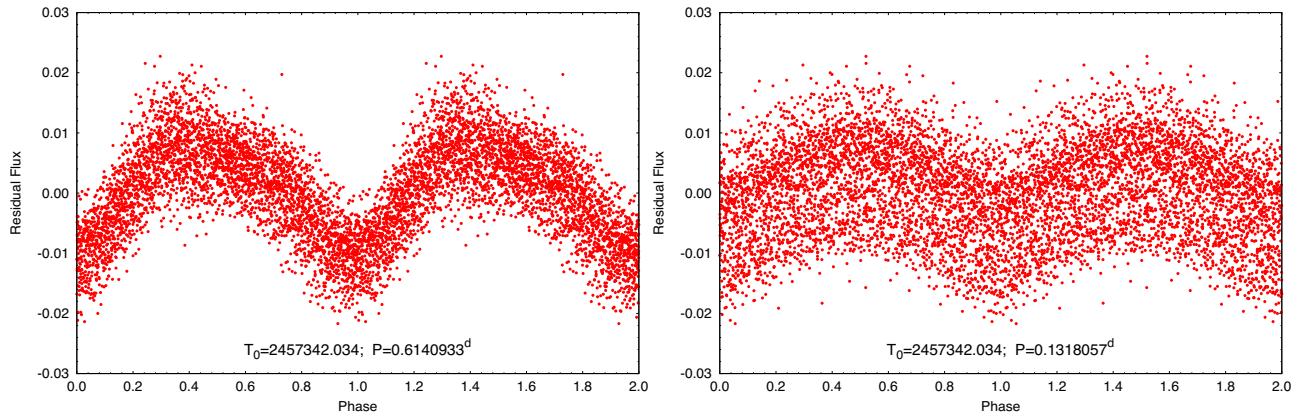


Figure 8. Folded light curves for periods of 0.6141 and 0.1318 d (left and right, respectively) after the best-fitting orbital light curves of the A and B binaries have been subtracted. The period in the left-hand panel is shorter than the orbital period of binary B by only ~ 5.75 min. We interpret this as star-spots from the B binary that are not quite corotating with the orbital period of 0.6182 d.

Table 7. Parameters from the double EB simultaneous light curve and SB1+SB1 RVs solution.

Parameter	Binary A		Binary B	
P (d)	3.594728 ± 0.000014		0.618214 ± 0.000005	
Semimajor axis (R_{\odot})	12.21 ± 0.19		3.65 ± 0.16	
i ($^{\circ}$)	89.50 ± 0.58		64.66 ± 0.56	
e	0		0	
ω ($^{\circ}$)	—		—	
$t_{\text{prim eclipse}}$ (BJD)	$245\,7341.9183 \pm 0.0002$		$245\,7342.0357 \pm 0.0003$	
γ (km s^{-1})	30.24 ± 0.08		27.47 ± 2.44	
$\dot{\gamma}$ (cm s^{-2})	0.0039 ± 0.0004		0.0287 ± 0.0105	
$f(m_2)$ (M_{\odot})	0.0863 ± 0.0005		0.0173 ± 0.0027	
Individual stars	A1	A2	B1	B2
Relative quantities				
Mass ratio ($q = m_2/m_1$)	0.56 ± 0.05		0.31 ± 0.03	
Fractional radius ^a (R/a)	0.0975 ± 0.0014	0.0604 ± 0.0014	0.3542 ± 0.0077	0.2647 ± 0.0077
Fractional luminosity	0.37602	0.0186	0.5416	0.0254
Extra light [I_x]			0.048 ± 0.030	
Physical quantities				
T_{eff}^b (K)	6473 ± 129	4421 ± 107	6931 ± 250	4163 ± 176
Mass ^c (M_{\odot})	1.21 ± 0.09	0.68 ± 0.03	1.30 ± 0.21	0.41 ± 0.07
Radius ^d (R_{\odot})	1.19 ± 0.03	0.74 ± 0.02	1.33 ± 0.06	1.04 ± 0.05
Luminosity (L_{\odot})	2.24 ± 0.20	0.19 ± 0.02	3.66 ± 0.61	0.29 ± 0.06
M_{bol}	3.87 ± 0.10	6.56 ± 0.12	3.33 ± 0.19	6.09 ± 0.22
$\log g$ (cgs)	4.37 ± 0.04	4.53 ± 0.02	4.33 ± 0.09	4.10 ± 0.09
$(v \sin i)_{\text{sync}}^e$ (km s^{-1})	16.8 ± 0.4	10.4 ± 0.3	95.6 ± 4.8	76.9 ± 4.0
$(M_V)_{\text{tot}}$			2.74 ± 0.12	
Distance ^f (pc)			870 ± 100	

^aPolar radii. ^b $T_{\text{eff, A1}}$ and its uncertainty were taken from the spectroscopic analysis and used as a Gaussian prior for this joint photometric + RV analysis; the other T_{eff} s were calculated from the adjusted temperature ratios. ^c m_{A1} and its uncertainty were taken from the spectroscopic analysis and used as a Gaussian prior; the other masses were calculated as described in Section 7.2. ^dStellar radii were derived from the volume-equivalent fractional radii (R/a) and the orbital separation. ^eProjected synchronized rotational velocities, calculated using the volume-equivalent radii. ^fDistance to the quadruple, calculated from the photometric distance modulus with the inclusion of an estimate of the interstellar extinction.

nents of binary B are $M_{B1} \simeq 1.33 \pm 0.21 M_{\odot}$, $R_{B1} \simeq 1.33 \pm 0.06 R_{\odot}$ and $M_{B2} \simeq 0.41 \pm 0.07 M_{\odot}$, $R_{B2} \simeq 1.04 \pm 0.05 R_{\odot}$. The larger uncertainties in the masses come mainly from the poorer quality RV curve, which did not allow for a well-determined spectroscopic mass function. Note, in particular, the greatly oversized radius of the low-mass secondary star compared to its nominal main-sequence radius. Thus, we provide a separate discussion of the likely evolutionary scenario for this system in Section 9.

8 CONSTRAINTS ON THE QUADRUPLE'S OUTER ORBIT

We now utilize what we have learned about the A and B binaries from the AO imaging, the RV measurements, and the photometric data to place a couple of significant constraints on the outer orbit of the quadruple system. There are five principal results that help to constrain the outer orbit: (1) upper limits on the angular separation, α , of binary A and binary B; (2) the difference in gamma velocities

between the two binaries, $\Delta\gamma \equiv \gamma_A - \gamma_B$; (3) the acceleration of the centre of mass of binary A, $\dot{\gamma}_A$; (4) upper limits on \dot{P}_A and \dot{P}_B from the photometric ETV curves; and (5) the inferred masses of all four stars in the binaries. It turns out that the limits on \dot{P} (item 4) are not significant compared to essentially the same constraint set by $\dot{\gamma}_A$, and we do not consider this any further.

The specific values of these constraints are as follows:

- (i) $\alpha < 0.05$ arcsec;
- (ii) $\Delta\gamma \equiv \gamma_A - \gamma_B = -1.4 \pm 2.2$ km s⁻¹;
- (iii) $\dot{\gamma}_A = 0.0024 \pm 0.0007$ cm s⁻²;
- (iv) $M_A = 2.00 \pm 0.06 M_\odot$ and $M_B = 1.88 \pm 0.06 M_\odot$.

We hereafter consider the masses of the A and B binaries to be the same to within their statistical uncertainties.

We now proceed to make use of these facts to constrain the outer orbit. For an arbitrary outer orbit, we can write down analytic expressions for α , $\Delta\gamma$, and $\dot{\gamma}_A$ (see also Lehmann et al. 2016; Rappaport et al. 2016):

$$\alpha = \frac{r}{d} \sqrt{1 - \sin^2 i \sin^2(\phi + \omega)}, \quad (3)$$

$$\Delta\gamma = \sqrt{\frac{GM_Q}{a(1-e^2)}} [\cos(\phi + \omega) + e \cos \omega] \sin i, \quad (4)$$

$$\dot{\gamma}_A = -\frac{GM_B}{r^2} \sin(\phi + \omega) \sin i. \quad (5)$$

The definitions of the quantities appearing in these equations for are: a , the semimajor axis; ϕ , the true anomaly; ω , the argument of periastron; e , the orbital eccentricity; and i , the orbital inclination angle, where all these quantities pertain explicitly to the outer orbit. The variable r is the orbital separation, given by the equation of an ellipse: $r = a(1 - e^2)/(1 + e \cos \phi)$. Further, M_Q and M_B are the total mass of the quadruple system and binary B, respectively, and d is the distance to the quadruple from the Earth.

There are five parameters of the outer orbit we would like to know (a , P , e , ω , and i), and only the four constraints listed above. Therefore, we will be able to set only ranges of acceptable values for some of these five parameters. The masses are used to relate a and P through Kepler's third law.

The approach we take to compute probability distributions for P , e , ω , and i is via Monte Carlo sampling of these parameters, as well as of the unknown instantaneous true anomaly, and then testing for each system realization whether the constraints for α , $\Delta\gamma$, and $\dot{\gamma}_A$ are satisfied to within their uncertainties, assuming Gaussian errors. For each realization, we randomly sample the mean anomaly in time, compute the corresponding eccentric anomaly, and from that the true anomaly, ϕ . Specifically we choose linear random values of P from 0 to 1000 yr, e from 0 to 1, and ω from 0 to 2π . The orbital inclination was chosen from a uniform probability per unit solid angle. Finally, the distance to the source was taken to be 870 pc with a Gaussian distribution with $\sigma = 100$ pc. The quantities α , $\Delta\gamma$, and $\dot{\gamma}_A$ are then evaluated via equations (3), (4), and (5) and are compared to the measured values.

Somewhat as we anticipated, the only outer orbit parameters for which interesting constraints could be set are P and a . Output histograms for P and a are shown in Fig. 9. For these two distributions we find that the outer period is most probably near 20 yr, but could reasonably be as short as 10 yr or as long as 80 yr. The corresponding semimajor axis of the quadruple is likely 18 ± 10 au. Therefore, in just a couple of additional seasons of either eclipse monitoring or follow-up RVs from this system, we can expect to see a significant

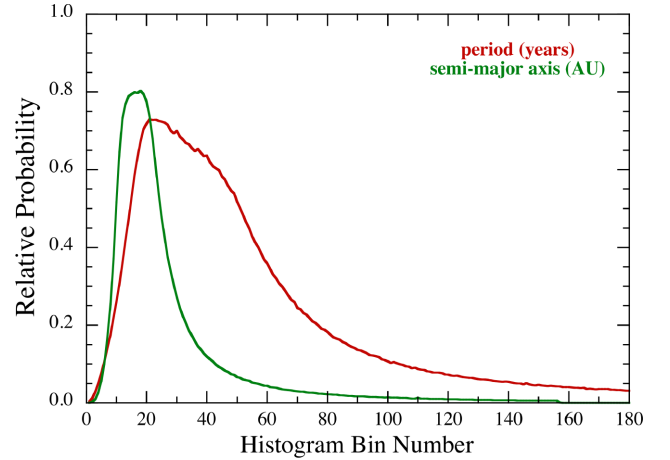


Figure 9. Output histograms for the period and semimajor axis associated with the outer orbit of the quadruple. See text, Section 8 for details of the Monte Carlo orbit sampling.

LTTE from the orbit and/or a much more significant determination of $\dot{\gamma}_A$.

9 EVOLUTION OF BINARY B

In this section we address the fact that the lower mass star in binary B appears to be the more evolved one. This implies that it is an Algol-like system and the lower mass star either has lost, or is continuing to lose, its envelope to the currently more massive star.

Since the properties of the components in binary B are reasonably well determined, this allows us to construct evolutionary scenarios that are self-consistent with the formation and evolution of EPIC 219217635 as a whole. Given the donor star's mass ($0.41 \pm 0.07 M_\odot$) and radius ($\simeq 1.04 \pm 0.05 R_\odot$) we conclude that the star is too large for its mass to be on the main sequence, and therefore must be substantially evolved. In fact, we believe that this star belongs to a class of stars known as 'stragglers' that have been previously studied by Kaluzny (2003), Orosz & van Kerkwijk (2003), and Mathieu et al. (2003). These stars are considerably redder than their main-sequence counterparts and likely experienced some nuclear burning before undergoing a phase of rapid mass loss (Case AB evolution). Thus red stragglers can be legitimately viewed as a special class of Algol-like binaries.

The general properties and evolution of Algol variables have been well studied (see e.g. Batten 1989, and references therein; Peters 2001). The more massive star in these systems fills its Roche lobe first and undergoes Roche lobe overflow (RLOF). A prolonged phase of stable (and sometimes rapid) mass transfer to the less massive companion often ensues. One of the difficulties in calculating this type of dynamically stable mass transfer arises from the problem of quantifying the degree to which the mass transfer is non-conservative (i.e. to determine the fraction of mass that is lost from the binary during RLOF). As has been shown by Eggleton (2000), a wide range of values is required in order to explain the observations of Algol-like systems (see also Nelson & Eggleton 2001). The secondary usually accretes enough matter so as to cause the mass ratio to become 'inverted' leading to a binary that contains a more evolved yet less massive primary star compared to the secondary star (accretor). Algol variables are normally observed as either being detached with both stars underfilling their respective Roche lobes, or semidetached with the donor star still undergoing

RLOF. The orbital periods of these binaries typically vary from $P_{\text{orb}} \gtrsim 1$ d to decades.

Red stragglers are likely low-mass stars that have evolved considerably (e.g. they may have consumed all of their central hydrogen) before filling their Roche lobes and undergoing a reasonably fast phase of thermal time-scale mass transfer to the accretor (see e.g. Zhou et al. 2018, and references therein). The subsequent evolution can be classified with reference to the bifurcation limit (Plyser & Savonije 1988). If mass is stripped rapidly enough, the binaries will evolve below the bifurcation limit and will attain orbital periods on the order of an hour (see e.g. Nelson, Dubeau & MacCannell 2004; Kalomeni et al. 2016). In this case the mass-loss time-scale of the binary is sufficiently short compared to the donor’s nuclear time-scale, although the donor star becomes chemically evolved, it cannot ascend the red giant branch (RGB). On the other hand, if the donor can evolve up the RGB while having its hydrogen-rich envelope stripped away, it will produce a helium white dwarf remnant (see e.g. Rappaport et al. 2015). For this latter case, the initial conditions of the progenitor binary allow it to produce a degenerate remnant and thus the binary lies above the bifurcation limit.

Because the components of binary A were formed coevally with those of binary B and given that the more massive component in A has a mass of $\simeq 1.2 M_{\odot}$ and shows little sign of significant nuclear evolution, we require that the progenitor primary of binary B had a mass of $\gtrsim 1.5 M_{\odot}$. The mass of the progenitor secondary in binary B is much less well constrained. It must be chosen to be significantly less than that of the primary so that it has not experienced significant nuclear (chemical) evolution and because the mass ratio $(M_{2,0}/M_{1,0})^{12}$ must not be so low as to cause a dynamical instability (leading to a possible merger). We found that progenitor masses of $M_{1,0} \approx 1.7 M_{\odot}$ and $M_{2,0} \approx 0.8 M_{\odot}$ worked reasonably well in reproducing the currently observed properties of binary B.

According to our preferred scenario, the progenitor binary consisted of an $\approx 1.7 M_{\odot}$ primary (the current donor star) and a relatively low-mass ($\approx 0.8 M_{\odot}$) secondary. After the primary has burned some of the hydrogen in its core, it undergoes RLOF on its thermal (Kelvin–Helmholtz) time-scale. This leads to relatively rapid transfer rates in excess of $10^{-7} M_{\odot} \text{ yr}^{-1}$. After more than one solar mass of material has been lost, the mass of the donor is reduced to the presently inferred value of $\approx 0.45 M_{\odot}$, while the companion’s mass increases to approximately $1.4 M_{\odot}$. Thus about 50 per cent of the transferred mass is lost from the binary in the form of a ‘fast’ Jeans wind (the expelled matter carries away the specific angular momentum of the accretor).

In order to test the robustness of the scenario, we created a small grid of evolutionary models using the MESA stellar evolution code (Paxton et al. 2011). The progenitor binary was assumed to have a solar metallicity ($Z = 0.02$) and the evolution was computed in accordance with the ‘standard’ RLOF model (Goliash & Nelson 2015) under the assumption of a ‘fast’ Jeans mode of systemic mass loss and allowing for gravitational radiation and magnetic braking angular momentum dissipation. Although highly uncertain, we set the systemic mass-loss parameters such that $\alpha = 0$ and $\beta = 0.5$ (see Tauris & van den Heuvel 2006, for a detailed explanation). This implies that no mass was ejected from the system directly from the primary, while 50 per cent of the mass passing through the inner

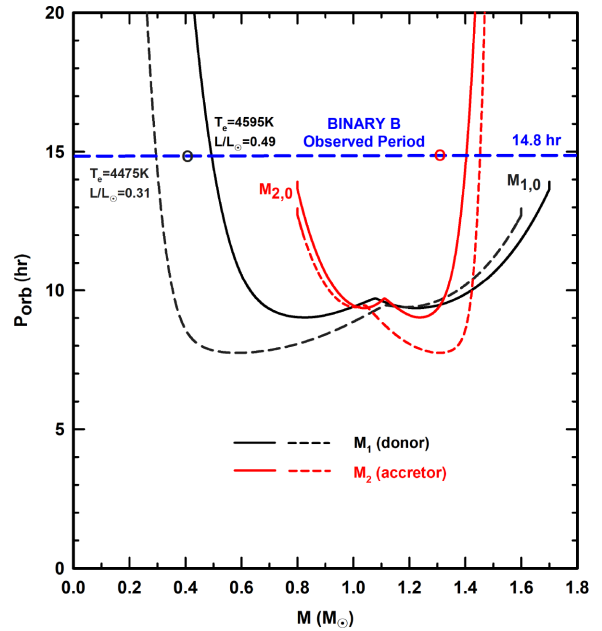


Figure 10. The evolution of representative models for binary B in the $P_{\text{orb}}-M$ plane. The black and red curves represent the evolution of the primary (donor) and secondary (accretor), respectively. The solid and dashed curves correspond to two different sets of initial conditions for the progenitor binary. The black and red circles denote the locations of the observationally inferred values of P_{orb} and M for the primary and secondary, respectively. Typical model ages at the current epoch are 2–3 Gyr.

Lagrange point to the secondary was subsequently ejected from the system. It should be noted that our ability to create models that approximately reproduce the properties of binary B does not depend sensitively on the choice of β . We found that adjusting the value of β up or down by ≈ 0.2 would still yield models with similar properties to those of binary B as long as the mass of the progenitor secondary was increased or reduced accordingly. Although the binary dynamics were computed self-consistently, the changes to the interior structure of each component were calculated independently. The evolutionary tracks were terminated once the secondary (accretor) had evolved sufficiently so as to fill its own Roche lobe.

Fig. 10 shows the evolutionary tracks in the $P_{\text{orb}}-M$ plane for two representative sets of initial conditions for the progenitor binary. Starting with $M_{1,0} = 1.7 M_{\odot}$ and $M_{2,0} = 0.8 M_{\odot}$, and an initial $P_{\text{orb}} = 14$ h, the computations imply present-day masses of 0.49 and $1.40 M_{\odot}$, respectively, at a $P_{\text{orb}} = 14.8$ h (solid black curve in Fig. 1). The value of P_{orb} is known extremely precisely, while the inferred values of the component masses given in Table 7 are less certain. The values of the computed masses are reasonably close to the inferred values for $P_{\text{orb}} = 14.8$ h. Because of the constraints of Roche geometry imposed on the lobe-filling donor (i.e. the dependence of R_1 on P_{orb} and M_1), the computed radius agrees with the inferred one to within ≈ 10 per cent. We also conclude that the value of $\log g$ is within 0.1 dex of the inferred value. The largest discrepancy can be found in the effective temperature of the donor star. Our computed T_{eff} is always about 500 K higher than the inferred value regardless of the initial conditions that we choose.¹³ As an illustration of this point, consider the dashed black track in

¹²For purposes of discussing the prior evolutionary history of binary B, we have reversed the labels ‘1’ and ‘2’, now referring to the originally more massive star as ‘1’ and vice versa.

¹³This may be an artefact of the uncertainty in the conversion of colours to temperatures.

Fig. 1. The initial mass of the primary was chosen to be $1.6 M_{\odot}$ and the initial period was $P_{\text{orb}} = 13$ h (the initial secondary mass was the same). According to this track the mass of the present-day donor is reduced to $0.30 M_{\odot}$ but the value of T_{eff} is only reduced by about 100 K. We could not find combinations of progenitor parameters (or variations in the input physics associated with systemic mass loss) that led to much smaller temperatures. As for the secondary, its computed mass is very close to the inferred value (see the solid red curve in Fig. 10). Since the calculated mass transfer rate for the observed orbital period is $\lesssim 10^{-9} M_{\odot} \text{ yr}^{-1}$, the secondary easily relaxes to its approximate thermal equilibrium configuration as it accretes matter. For the present day, our calculations show that the secondary underfills its Roche lobe by nearly a factor of 2. For a mass of $1.4 M_{\odot}$, we find that its temperature is close to 6600 K and the radius is about $1.6 R_{\odot}$. These values are not significantly different from those given in Table 7. We also find that of the progenitor models that can reasonably explain the currently observed system properties, evolutionary ages ranged between ~ 2 and 3 Gyr.

According to our proposed scenario, the progenitor primary experiences a phase of rapid mass loss on its Kelvin time while the value of the mass ratio (M_2/M_1) is $\lesssim 1$. When the donor's mass is thus reduced to less than $1 M_{\odot}$, it starts to evolve on a nuclear time-scale and the radius of the donor increases (as does P_{orb}). Although this binary evolves above the bifurcation limit (i.e. the donor would eventually become a giant and collapse to become a helium white dwarf), the increase in the mass of the secondary allows it to evolve and fill its Roche lobe before the donor can become a giant. This might lead to a reversal in the direction of mass transfer or a merger might ensue. Regardless of the possible future evolution, we feel confident in stating that the evolution of binary B can be explained without the need to invoke a phase of common envelope evolution. If this is true, then the study of the evolution of binaries A and B can be carried out independently.

10 SUMMARY AND CONCLUSIONS

In this work we have identified a physically bound quadruple system composed of two short-period EBs in an ~ 20 au orbit about each other. The doubly eclipsing system was found in Field 7 of the K2 mission, with periods of $P_A \simeq 3.5949$ d and $P_B \simeq 0.6182$ d.

We acquired follow-up ground-based observations including (1) Keck AO images showing that the separation between the two binaries is $\lesssim 0.05$ arcsec; (2) 20 radial velocity measurements with the NOT-FIES spectrometer that yield single-line RV curves for both binaries; and (3) photometry with small-aperture telescopes (12–14 inch) that yielded nine additional eclipse times, thereby increasing the overall observation interval to nearly 2 yr.

We analyse the photometric and radial velocity data for both binaries all simultaneously to yield many of the binary system parameters. The results are summarized in Table 7.

The ETVs of both binaries show erratic behaviour (binary B) or non-secular trends (binary A), and these are not associated with any LTTEs or physical interactions between the binaries.

We set significant constraints on the outer (i.e. quadruple) orbit using the AO and RV measurements. These indicate that the semi-major axis of the outer orbit is 18 ± 10 au with a likely outer period of 20–40 yr.

The upper limit to the angular separation (from the AO image), the nearly matching γ velocities, and the similar luminosities of the two binaries provide compelling *circumstantial* evidence for the physical association of the two binaries. By contrast, the detection,

at the 3.2σ confidence level, of $\dot{\gamma}$ for the binary A is important *direct* evidence that the binaries are physically interacting with one another.

If a few further RV measurements can be made over the next year, the significance of the $\dot{\gamma}$ detection can be made much stronger. As discussed in the Introduction, there are only a relative handful of double eclipsing quadruples known to be physically bound, and EPIC 219217635 is nearly certain to join their ranks.

We have demonstrated that the target is sufficiently bright for small (i.e. 12–14-inch class) telescopes to continue to follow the timing of the primary eclipses of both binaries. At some point, the light travel time delays in the system will begin to dominate over the more erratic ETV behaviour, and would also allow for a more definitive measure of the outer orbit. For example, in the case of a circular outer orbit having a period of $P_{\text{out}} \approx 20$ yr, and therefore, an orbital separation of $a_{\text{out}} \approx 12$ au one can expect periodic ETVs for both binaries with almost equal semi-amplitudes of $\mathcal{A}_{\text{LTTE}} \approx 50 \times \sin i_{\text{out}}$ min, and of course with opposite phases. Or, from a different perspective, converting the variation of the systemic RV of binary A obtained from our analysis (see Section 6), i.e. $\dot{\gamma} = 0.0024 \pm 0.0007 \text{ cm s}^{-2}$ into a period variation rate, one gets $\Delta P_A = 8.8 \pm 2.5 \times 10^{-8} \text{ d cycle}^{-1}$. Assuming that this value is approximately constant over an interval that is much shorter than the outer orbital period, we find that the expected difference of the observed and linearly predicted eclipse times after N inner orbital cycles can be calculated as

$$\Delta t \approx \frac{1}{2} \Delta P \times N^2. \quad (6)$$

From this, one can easily show that it is inevitable that there will be an observable 15-min shift in the eclipse times after only $N \approx 477$ cycles, i.e. ≈ 4.7 yr. Therefore, we can expect definite confirmation of the gravitationally bound nature of this quadruple within a few years.

Note also that accurate future observations of the complete LTTE orbits of the two binaries will offer all of the benefits that can be obtained from RV measurements of a double-lined spectroscopic binary. And, in addition, because the masses of the two binaries are known relatively well, one will also be able to calculate from the LTTE amplitudes the observed inclination (i_{out}) of the outer orbit.

We would also like to suggest that a few additional RV measurements be made for the next few observing seasons for this system. For outer orbital periods of ~ 20 yr, the value of $\dot{\gamma}_A$ would not only be firmed up, but within just a few more years, the curvature of the outer orbit should be detected.

Finally, from our analysis, B binary appears to have its less massive and cooler star evolved well beyond where its main-sequence radius would be, and is filling (or nearly filling) its Roche lobe. We describe a possible evolutionary path to explain this apparent very short period Algol-like red straggler system.

ACKNOWLEDGEMENTS

We are grateful to Jules Halpern for acquiring an initial image of the field at the MDM Observatory. TB acknowledges the financial support of the Hungarian National Research, Development and Innovation Office – NKFIH Grant OTKA K-113117. SA and ABJ acknowledge support by the Danish Council for Independent Research, through a DFF Sapere Aude Starting Grant No. 4181-00487B. AV's work was supported in part under a contract with the California Institute of Technology (Caltech)/Jet Propulsion Laboratory (JPL) funded by NASA through the Sagan Fellowship Program

executed by the NASA Exoplanet Science Institute. MHK, DLC, and T L J acknowledge Allan R. Schmitt for making his light-curve examining software ‘LCTOOLS’ freely available. LN thanks A. Senhadji for technical assistance and the Natural Sciences and Engineering Research Council (Canada) for financial support provided through a Discovery Grant. We also thank Calcul Québec, the Canada Foundation for Innovation (CFI), NanoQuébec, RMGA, and the Fonds de recherche du Québec – Nature et technologies (FRQNT) for computational facilities. The radial velocity spectral observations were made with the Nordic Optical Telescope (NOT), operated by the Nordic Optical Telescope Scientific Association at the Observatorio del Roque de los Muchachos, La Palma, Spain, of the Instituto de Astrofísica de Canarias. The authors are grateful to Davide Gandolfi for time sharing some of his NOT observations between programs. Some of the data presented in this paper were obtained from the Mikulski Archive for Space Telescopes (MAST). STScI is operated by the Association of Universities for Research in Astronomy, Inc., under NASA contract NAS5-26555. Support for MAST for non-*HST* data is provided by the NASA Office of Space Science via grant NNX09AF08G and by other grants and contracts. A portion of this work was based on observations at the W. M. Keck Observatory granted by the California Institute of Technology. We thank the observers who contributed to the measurements reported here and acknowledge the efforts of the Keck Observatory staff. We extend special thanks to those of Hawaiian ancestry on whose sacred mountain of Mauna Kea we are privileged to be guests. Some results are based on data from the Carlsberg Meridian Catalogue 15 Data Access Service at CAB (INTA-CSIC). This paper includes data collected by the Kepler mission. Funding for the Kepler mission is provided by the NASA Science Mission directorate.

REFERENCES

- Ahn C. P. et al., 2012, *ApJS*, 203, 21
 Auvergne M. et al., 2009, *A&A*, 506, 411
 Avni Y., 1976, *ApJ*, 209, 574
 Bagnuolo W. G., Jr, Gies D. R., 1991, *ApJ*, 376, 266
 Balaji B., Croll B., Levine A. M., Rappaport S., 2015, *MNRAS*, 448, 429
 Batten A. H., 1989, *Space Sci. Rev.*, 50, 1
 Batten A. H., Hardie R. H., 1965, *AJ*, 70, 666
 Blanco-Cuaresma S., Soubiran C., Heiter U., Jofré P., 2014, *A&A*, 569, A111
 Borkovits T., Hajdu T., Sztakovics J., Rappaport S., Levine A., Bíró I. B., Klagyivik P., 2016, *MNRAS*, 455, 4136
 Borkovits T. et al., 2013, *MNRAS*, 428, 1656
 Borucki W. J. et al., 2010, *Science*, 327, 977
 Cagaš P., Pejcha O., 2012, *A&A*, 544, L3
 Castelli F., Kurucz R. L., 2004, preprint ([arXiv:astro-ph/0405087](https://arxiv.org/abs/astro-ph/0405087))
 Cutri R. M. et al., 2013, Explanatory Supplement to the AllWISE Data Release Products, Technical Report, p. 1
 De Rosa R. J. et al., 2014, *MNRAS*, 437, 1216
 Eggleton P. P., 2000, *New Astron. Rev.*, 44, 111
 Eggleton P. P., Kiseleva-Eggleton L., 2001, *ApJ*, 562, 1012
 Erikson A. et al., 2012, *A&A*, 539, A14
 Fabrycky D., Tremaine S., 2007, *ApJ*, 669, 1298
 Fang X., Thompson T. A., Hirata C. M., 2018, *MNRAS*, 476, 4234
 Fernández Fernández J., Chou D.-Y., 2015, *PASP*, 127, 421
 Flower P. J., 1996, *ApJ*, 469, 355
 Ford E. B., 2005, *AJ*, 129, 1706
 Frandsen S., Lindberg B., 1999, in Karttunen H., Pirola V., eds, *Astrophysics with the NOT*. University of Turku, Tuorla Observatory, Piikkiö, Finland, p. 71
 Goliasch J., Nelson L., 2015, *ApJ*, 809, 80
 Gray R. O., Corbally C. J., 1994, *AJ*, 107, 742
 Guver T., Özel F., 2009, *MNRAS*, 400, 2050
 Hajdu T., Borkovits T., Forgács-Dajka E., Sztakovics J., Marschalló G., Benkő J. M., Klagyivik P., Sallai M. J., 2017, *MNRAS*, 471, 1230
 Helminiak K. G., Ukita N., Kambe E., Kozłowski S. K., Pawłaszek R., Maehara H., Baranec C., Konacki M., 2017, *A&A*, 602, A30
 Hong K. et al., 2018, *PASP*, 130, 054204
 Huber D. et al., 2016, *ApJS*, 224, 2
 Husser T.-O., Wende-von Berg S., Dreizler S., Homeier D., Reiners A., Barman T., Hauschildt P. H., 2013, *A&A*, 553, A6
 Kalomeni B., Nelson L., Rappaport S., Molnar M., Quintin J., Yakut K., 2016, *ApJ*, 833, 83
 Kaluzny J., 2003, *Acta Astron.*, 53, 51
 Kipping D. M. et al., 2015, *ApJ*, 813, 14
 Kopal Z., 1989, *The Roche Problem and Its Significance for Double-Star Astronomy*. Astrophysics and Space Science Library, Vol. 152. Kluwer, Dordrecht
 Kovács G., Zucker S., Mazeh T., 2002, *A&A*, 391, 369
 Kozai Y., 1962, *AJ*, 67, 591
 Lee C.-U., Kim S.-L., Lee J. W., Kim C.-H., Jeon Y.-B., Kim H.-I., Yoon J.-N., Humphrey A., 2008, *MNRAS*, 389, 1630
 Lehmann H., Borkovits T., Rappaport S., Ngo H., Mawet D., Cszimadia Sz., Forgács-Dajka E., 2016, *ApJ*, 819, 33
 Lehmann H., Zechmeister M., Dreizler S., Schuh S., Kanzler R., 2012, *A&A*, 541, A105
 Lidov M. L., 1962, *Planet. Space Sci.*, 9, 719
 Lindegren L. et al., 2018, preprint ([arXiv:1804.09366](https://arxiv.org/abs/1804.09366))
 Loeb A., Gaudi B. S., 2003, *ApJ*, 588, 117
 Lohr M. E. et al., 2015, *A&A*, 578, A103
 Mathieu R. D., van den Berg M., Torres G., Latham D., Verbunt F., Stassun K., 2003, *AJ*, 125, 246
 Naoz S., Fabrycky D. C., 2014, *ApJ*, 793, 137
 Nelson C., Eggleton P. P., 2001, *ApJ*, 552, 664
 Nelson L. A., Dubeau E. P., MacCannell K. A., 2004, *ApJ*, 616, 1124
 Ngo H. et al., 2015, *ApJ*, 800, 138
 Orosz J. A., van Kerkwijk M. H., 2003, *A&A*, 397, 237
 Paxton B., Bildsten L., Dotter A., Herwig F., Lesaffre P., Timmes F., 2011, *ApJS*, 192, 3
 Pejcha O., Antognini J. M., Shappee B. J., Thompson T. A., 2013, *MNRAS*, 435, 943
 Perets H. B., Fabrycky D. C., 2009, *ApJ*, 697, 1048
 Peters G. J., 2001, in Vanbeveren D., ed., *The Influence of Binaries on Stellar Population Studies*. Astrophysics and Space Science Library, Vol. 264. Kluwer, Dordrecht, p. 79
 Pietrinferni A., Cassisi S., Salaris M., Castelli F., 2004, *ApJ*, 612, 168
 Pietrukowicz P. et al., 2013, *Acta Astron.*, 63, 115
 Pollacco D. L. et al., 2006, *PASP*, 118, 1407
 Prša A., Zwitter T., 2005, *ApJ*, 628, 426
 Pylyser E., Savonije G. J., 1988, *A&A*, 191, 57
 Rappaport S., Nelson L., Levine A., Sanchis-Ojeda R., Gandolfi D., Nowak G., Palle E., Prša A., 2015, *ApJ*, 803, 82
 Rappaport S. et al., 2016, *MNRAS*, 462, 1812
 Rappaport S. et al., 2017, *MNRAS*, 467, 2160
 Service M., Lu J. R., Campbell R., Sitariski B. N., Ghez A. M., Anderson J., 2016, *PASP*, 128, 5004
 Shibahashi H., Kurtz D. W., 2012, *MNRAS*, 422, 738
 Silva Aguirre V. et al., 2015, *MNRAS*, 452, 2127
 Skrutskie M. F. et al., 2006, *AJ*, 131, 1163
 Smart R. L., Nicasastro L., 2014, *A&A*, 570, A87
 Szabados L., 1997, in Battrick B., ed., *Proceedings of the ESA Symposium ‘Hipparcos – Venice ‘97’*, ESA SP-402. ESA, Noordwijk, p. 657
 Tauris T. M., van den Heuvel E. P. J., 2006, in Lewin W. H. G., van der Klis M., eds, *Compact Stellar X-ray Sources*. Cambridge Univ. Press, Cambridge, p. 623
 Teltung J. H. et al., 2014, *Astron. Nachr.*, 335, 41
 Terrell D., Wilson R. E., 2005, *Ap&SS*, 296, 221
 Tokovinin A., 2008, *MNRAS*, 389, 925
 Tokovinin A., 2014, *AJ*, 147, 87

- Tokovinin A., 2018, *AJ*, 155, 160
Torres G., 2010, *AJ*, 140, 1158
Torres G., Sandberg Lacy C. H., Fekel F. C., Wolf M., Muterspaugh M. W., 2017, *ApJ*, 846, 115
Tout C. A., Pols O. R., Eggleton P. P., Han Z., 1996, *MNRAS*, 281, 257
Tran K., Levine A., Rappaport S., Borkovits T., Csizmadia Sz., Kalomeni B., 2013, *ApJ*, 774, 81
Vanderburg A., Johnson J. A., 2014, *PASP*, 126, 948
van Kerkwijk M. H., Rappaport S., Breton R., Justham S., Podsiadlowski Ph., Han Z., 2010, *ApJ*, 715, 51
Wilson R. E., 1979, *ApJ*, 234, 1054
Wilson R. E., 1994, *PASP*, 106, 921
Zacharias N., Finch C. T., Girard T. M., Henden A., Bartlett J. L., Monet D. G., Zacharias M. I., 2013, *ApJS*, 145, 44
Zasche P., Uhlář R., 2016, *A&A*, 588, A121
Zhou G. et al., 2018, *ApJ*, 854, 109

APPENDIX A: MASS AND TEMPERATURE INFORMATION FROM JOINT PHOTOMETRIC SOLUTION

Here we show that the depth of the primary eclipse in binary A has encoded in it information about either the mass ratio of the two binaries or the temperature ratio of the primary stars in the two different binary subsystems. We start by writing down an expression for the depth of the primary eclipse, D_{A1} , of binary A, which is a complete transit. For simplicity, we take the stars to (1) be spherical, and can thereby represent area ratios as e.g. $(R_{A2}/R_{A1})^2$, and (2) have surface a brightness proportional to T_{eff}^4 . However, the derivation would be the same if we did the exercise for stars whose surfaces follow Roche geometry and have their fluxes measured through specific filter bands, and are subject to limb darkening and other higher order effects. Furthermore, we also assume that any ‘third-light’ contribution, exterior to the quadruple, is negligible:

$$D_{A1} \simeq \frac{R_{A2}^2 T_{A1}^4}{R_{A1}^2 T_{A1}^4 + R_{A2}^2 T_{A2}^4 + R_{B1}^2 T_{B1}^4 + R_{B2}^2 T_{B2}^4}. \quad (\text{A1})$$

Dividing by $R_{A1}^2 T_{A1}^4$ yields

$$D_{A1} \simeq \frac{(R_{A2}/R_{A1})^2}{1 + (R_{A2}/R_{A1})^2(T_{A2}/T_{A1})^4 + (R_{B1}/R_{A1})^2(T_{B1}/T_{A1})^4 + (R_{B2}/R_{A1})^2(T_{B2}/T_{A1})^4}. \quad (\text{A2})$$

Finally, if we write the scaled radii as lower case ‘ r ’ e.g. $r_{A1} \equiv R_{A1}/a_A$, where a_A is the semimajor axis of binary A, then the above expression can be written as

$$D_{A1} \simeq \frac{(r_{A2}/r_{A1})^2}{1 + (r_{A2}/r_{A1})^2(T_{A2}/T_{A1})^4 + (a_B/a_A)^2(r_{B1}/r_{A1})^2(T_{B1}/T_{A1})^4 \{1 + (r_{B2}/r_{B1})^2(T_{B2}/T_{B1})^4\}}, \quad (\text{A3})$$

where all of the terms in this expression are determined directly from the photometric analysis, except for the terms (a_B/a_A) and (T_{B1}/T_{A1}) in bold face that are the ratio of physical semimajor axes of the two binaries and the ratio of the effective temperatures of the two primaries. Thus, in principle, the simultaneous photometric solution of the two binaries contains information not just on radius and temperature ratios, but also on the ratio of semimajor axes, and hence the mass ratio of the two binaries.

¹Baja Astronomical Observatory of Szeged University, Szegedi út, Kt. 766, H-6500 Baja, Hungary

²Konkoly Observatory, Research Centre for Astronomy and Earth Sciences, Hungarian Academy of Sciences, Konkoly Thege Miklós út 15-17, H-1121 Budapest, Hungary

³Stellar Astrophysics Centre, Department of Physics and Astronomy, Aarhus University, Ny Munkegade 120, DK-8000 Aarhus C, Denmark

⁴Department of Physics, and Kavli Institute for Astrophysics and Space Research, M.I.T., Cambridge, MA 02139, USA

⁵Department of Physics and Astronomy, Bishop’s University, 2600 College St., Sherbrooke, QC J1M 1Z7, Canada

⁶Harvard-Smithsonian Center for Astrophysics, 60 Garden Street, Cambridge, MA 02138, USA

⁷Department of Astronomy, The University of Texas at Austin, 2515 Speedway, Stop C1400, Austin, TX 78712, USA

⁸Hereford Arizona Observatory, Hereford, AZ 85615, USA

⁹Perth Exoplanet Survey Telescope, Perth, Western Australia 6010, Australia

¹⁰DTU Space, National Space Institute, Technical University of Denmark, Elektrovej 327, DK-2800 Lyngby, Denmark

¹¹Brorfelde Observatory, Observator Gyldenkerne Vej 7, DK-4340 Tølløse, Denmark

¹²12812 SE 69th Place Bellevue, WA 98006, USA

¹³7507 52nd Place NE Marysville, WA 98270, USA

¹⁴NRC Canada Herzberg Astronomy and Astrophysics, Victoria, BC V9E 2E7, Canada

¹⁵Division of Geological and Planetary Sciences, California Institute of Technology, Pasadena, CA 91125, USA

¹⁶Department of Astronomy, California Institute of Technology, Pasadena, CA 91125, USA

¹⁷Department of Astronomy and Jet Propulsion Laboratory, California Institute of Technology, Pasadena, CA 91125, USA

¹⁸Space Science and Astrobiology Division, NASA Ames Research Center, M/S 245-1, Moffett Field, CA 94035, USA

¹⁹DTU Space, National Space Institute, Technical University of Denmark, Elektrovej 328, DK-2800 Kgs. Lyngby, Denmark

²⁰Nordic Optical Telescope, Rambla José Ana Fernández Pérez 7, E-38711 Breña Baja, Spain

This paper has been typeset from a \LaTeX file prepared by the author.